Energetics and vortex structures near small-scale shear layers in turbulence

Tomoaki Watanabe (渡邉 智昭) and Koji Nagata (長田 孝二)

View Online   Export Citation   CrossMark

Energetics and vortex structures near small-scale shear layers in turbulence

View Online   Export Citation   CrossMark

Tomoaki Watanabe (渡邊 智昭),[1,a] (iD) and Koji Nagata (長田 孝二)[2] (iD)

AFFILIATIONS

[1]Education and Research Center for Flight Engineering, Nagoya University, Furo-cho, Chikusa, Nagoya 464-8603, Japan
[2]Department of Aerospace Engineering, Nagoya University, Furo-cho, Chikusa, Nagoya 464-8603, Japan

[a]Author to whom correspondence should be addressed: watanabe.tomoaki@c.nagoya-u.jp

ABSTRACT

Vortices and kinetic energy distributions around small-scale shear layers are investigated with direct numerical simulations of isotropic turbulence. The shear layers are examined with the triple decomposition of a velocity gradient tensor. The shear layers subject to a biaxial strain appear near vortices with rotation, which induce energetic flow that contributes to the shear. A similar configuration of rotating motions near the shear layers is observed in a multi-scale random velocity field, which is free from the dynamics of turbulence. Therefore, the mechanism that sustains shearing motion is embedded as a kinematic nature in random velocity fields. However, the biaxial strain is absent near the shear layers in random velocity because rotating motions appear right next to the shear layers. When a random velocity field begins to evolve following the Navier–Stokes equations, the shear layers are immediately tilted to the nearby rotating motions. This misalignment is a key for the vortex to generate the compressive strain of the biaxial strain around the shear layer. As the configuration of shearing and rotating motions arises from the kinematic nature, the shear layers with the biaxial strain are formed within a few times the Kolmogorov timescale once the random velocity field begins to evolve. The analysis with high-pass filtered random velocity suggests that this shear layer evolution is caused by small-scale turbulent motions. These results indicate that the kinematic nature of shear and rotation in velocity fluctuations has a significant role in the formation of shear layers in turbulence.

I. INTRODUCTION

Turbulence plays an important role in the flows encountered in various physical and engineering problems. Turbulence comprises fluid motions with a wide range of length scales, where the kinetic energy of large-scale motions is, on average, transferred to smaller scales and is dissipated by viscous effects at the small scales.[1] The small-scale fluid motions are also important in heat transfer and mixing of substances and cause the amplification of temperature and concentration gradients, which enhances heat conduction and molecular diffusion.[2] Small-scale properties of turbulence can be studied by analyzing quantities related to the velocity gradient tensor $\nabla \boldsymbol{u}$.[3] Throughout this paper, components of second-order tensors are denoted by subscripts, for example, $(\nabla \boldsymbol{u})_{ij} = \partial u_i / \partial x_j$, while tensors themselves are written without subscripts. For example, small-scale intermittency is investigated with the statistics of kinetic energy dissipation rate ε and enstrophy $\omega^2/2$, which are defined as $\varepsilon = 2\nu S_{ij} S_{ij}$ and $\omega^2/2 = \Omega_{ij}\Omega_{ij}$ with the kinematic viscosity ν, the rate-of-strain tensor $S_{ij} = [(\nabla \boldsymbol{u})_{ij} + (\nabla \boldsymbol{u})_{ji}]/2$ and the rate-of-rotation tensor $\Omega_{ij} = [(\nabla \boldsymbol{u})_{ij} - (\nabla \boldsymbol{u})_{ji}]/2$.[4,5]

The studies of small-scale properties of turbulence often concern turbulent structures, which can be perceivable as coherent patterns in flow visualization. One of the most well-known turbulent structures is the vortex tube.[6,7] Intense vortex tubes can be easily detected as flow regions with large enstrophy and have been extensively studied in different turbulent flows.[8–11] The vortex tubes are small-scale structures with a diameter close to 10 times the Kolmogorov scale. Another turbulent structure identified with enstrophy is a vortex sheet, which is a layer with moderately large enstrophy.[12] The vortex sheet can be characterized by intense shear and has also been called a shear layer in recent studies.[13,14] In this paper, we also name these structures shear layers because they are identified based on the local intensity of shearing motion. The properties of the flow regions occupied by the shear layers have been studied by identifying the location of shear layers.[15,16] These studies suggest that the shear layers are dynamically important because of their contribution to the evolution of turbulent kinetic energy and enstrophy.[16] However, the flow topology around shear layers has not been understood well because most identification schemes do not provide the orientation of shear layers. This is contrary
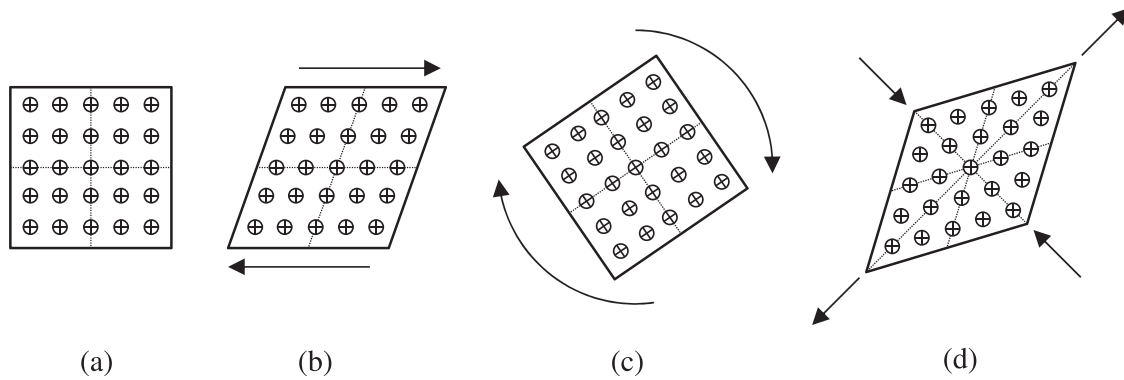
FIG. 1. Local fluid motions considered in the triple decomposition: (a) fluid element; (b) pure shearing; (c) rigid-body rotation; and (d) elongation (irrotational strain).

to vortex tubes, which have been investigated with averages taken as functions of a radial distance from the vortex center.[11] The radial direction can be identified on a plane normal to a vorticity vector. A similar statistical analysis for shear layers requires identification of the shear orientation.

A. The triple decomposition of velocity gradient tensor

Several new approaches to analyzing the velocity gradient tensor have been proposed in recent studies of vortex identification. The triple decomposition and the Rortex-based decomposition can decompose a vorticity field into the contributions from pure rotation and shear.[17,18] These decompositions concerning shearing motion are often used in the studies of flow structures and local flow topology.[13,14,19–27] The triple decomposition considers three motions of pure shearing (S), rigid-body rotation (R), and elongation (E), which are illustrated in Fig. 1 and decomposes ∇u into three components as $\nabla u = \nabla u_S + \nabla u_R + \nabla u_E$. Here, the intensities of the three motions are defined as $I_S = \sqrt{2(\nabla u_S)_{ij}(\nabla u_S)_{ij}}$, $I_R = \sqrt{2(\nabla u_R)_{ij}(\nabla u_R)_{ij}}$, and $I_E = \sqrt{2(\nabla u_E)_{ij}(\nabla u_E)_{ij}}$. It was shown that I_S and I_R are useful to detect shear layers and vortex tubes, respectively.[14,17,19,28,29]

The triple decomposition for a two-dimensional flow is described here to provide the basic concept. The triple decomposition is applied in a so-called basic reference frame, which can be related to the principal axes in a two-dimensional incompressible flow. The decomposition is straightforward for a two-dimensional flow because the basic reference frame is related to the principal axes of the rate-of-strain tensor. Although the triple decomposition is formulated for a three-dimensional flow, a more complicated procedure to identify the basic reference frame is required as discussed in Sec. III. In a two-dimensional incompressible flow, $(\nabla u)_{ij} = \partial u_i / \partial x_j$ with $i, j = 1, 2$ is written as

$$\nabla u = \begin{pmatrix} \partial u_1/\partial x_1 & \partial u_1/\partial x_2 \\ \partial u_2/\partial x_1 & -\partial u_1/\partial x_1 \end{pmatrix}. \tag{1}$$

The rate-of-strain tensor for Eq. (1) has two eigenvalues $s_1 = s$ and $s_2 = -s$, for which the eigenvectors are denoted by e_1 and e_2,

respectively. The basic reference frame is obtained by rotating the reference frame defined with the principal axes, e_1 and e_2, by $45°$. This relation between the principal axes and the basic reference frame is illustrated in Fig. 2, where the basic reference frame is expressed with the unit vectors b_1 and b_2. Here, the velocity gradient tensors in the reference frame of the principal axes and in the basic reference frame are denoted by $(\nabla u)^P$ and $(\nabla u)^B$, respectively, and are expressed as

$$(\nabla u)^P = \begin{pmatrix} s & -\omega \\ \omega & -s \end{pmatrix}, \quad (\nabla u)^B = \begin{pmatrix} 0 & s-\omega \\ s+\omega & 0 \end{pmatrix}. \tag{2}$$
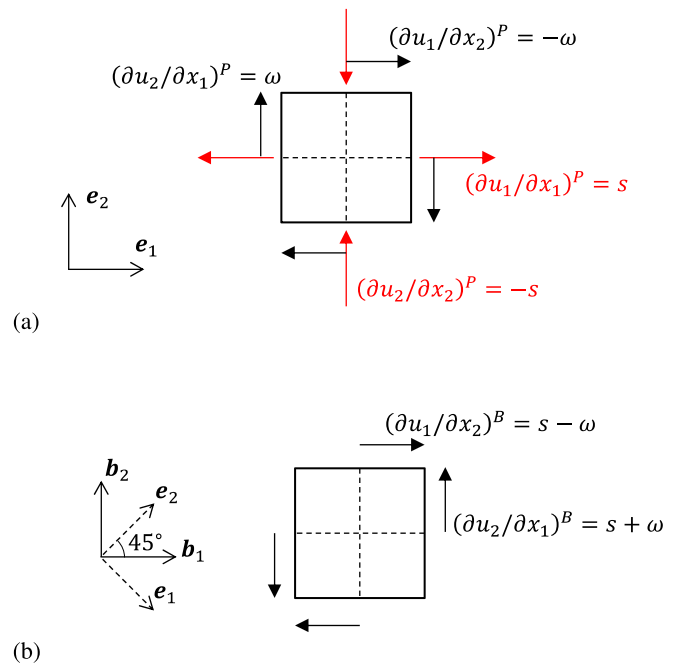

FIG. 2. The relation between (a) the reference frame of principal axes and (b) the basic reference frame.

Here, the length and direction of the arrows in Fig. 2 do not represent the magnitude and sign of the velocity gradients. Depending on the balance between ω and s, different local flow patterns are observed in the basic reference frame in Fig. 2(b), for example, rigid-body rotation, pure shearing, irrotational strain, and pure shearing with another motion. The detailed classification of the local flow patterns can be found in Ref. 17. In the basic reference frame, the shear tensor is given by

$$(\nabla \boldsymbol{u}_S)_{ij}^B = (\nabla \boldsymbol{u})_{ij}^B - \text{sgn}\left[(\nabla \boldsymbol{u})_{ij}^B\right] \min\left[|(\nabla \boldsymbol{u})_{ij}^B|, |(\nabla \boldsymbol{u})_{ji}^B|\right], \quad (3)$$

where $\text{sgn}(x)$ is the sign function defined as $\text{sgn}(x) = 1$ for $x \geq 0$ and $\text{sgn}(x) = -1$ for $x < 0$. The tensors for rotation and elongation are obtained as symmetric and antisymmetric parts of the residual tensor $(\nabla \boldsymbol{u})^B - (\nabla \boldsymbol{u}_S)^B$. The decomposition with Eq. (3) in the basic reference frame can effectively distinguish the three motions.

B. Application of the triple decomposition to study shear layers in turbulence

A new identification scheme of the shear layers has been developed with the triple decomposition since I_S is useful to detect shear layers. Furthermore, the shear tensor can be used to identify the orientation of each shear layer. A conditional averaging procedure[30–35] combined with the identification scheme of shear layers by the triple decomposition has been used to investigate the flow field around the shear layers. First, the shear layers detected with the triple decomposition have been investigated on a two-dimensional plane because the decomposition is easily applied to two-dimensional components of the velocity gradient tensor.[28] Then, the triple decomposition for the full components of $\nabla \boldsymbol{u}$ has been applied to three-dimensional turbulent flows for investigating the three-dimensional features of shear layers in isotropic turbulence, turbulent jets, and mixing layers.[14,29] Prior to these applications to the shear layer analysis, the triple decomposition has also been used to detect vortices in three-dimensional flows.[36,37] It has been shown that the velocity jump and the thickness of the shear layers are characterized by the Kolmogorov velocity and length scales, respectively.[13,14]

The recent advancement in the identification methods of shear layers enables us to reveal the characteristics of shear layers. However, the above examples of the analysis based on the triple decomposition are limited mostly to the mean flow topology and the length and velocity scalings. Of great interest is the mechanism that generates or sustains the shear layers in turbulent flows. The mean flow analysis indicates that the shear layers appear between two parallel flows in the

opposite direction.[13,14] Therefore, the process by which the shear layers are generated and sustained may be understood as the generation of energetic fluid motions in the proximity of the shear layers. It is also known that the shear layers appear near vortex tubes,[15,16] and from the viewpoint of turbulent structures, one may expect that the vortex tubes play an important role in the generation of shear layers. To address these issues related to the shear layers, we analyze direct numerical simulation (DNS) databases of isotropic turbulence with a special focus on the relation of shear layers and vortex tubes to the kinetic energy transport. The present study also uses the triple decomposition to evaluate the statistics of shear layers in relation to the shear orientation. Isotropic turbulence is compared with a multi-scale random velocity field that does not obey the Navier–Stokes equations. Comparison between genuine turbulence and random velocity is useful to reveal the kinematic nature of velocity fluctuations, which is free from the dynamics of turbulence.[38,39] Furthermore, DNS of decaying turbulence initialized with a random velocity field is also conducted to investigate the generation of shear layers from the structureless random velocity field.

The remainder of this paper is organized as follows: The details of DNS and random velocity are provided in Sec. II. Section III describes the method to analyze the shear layers. Section IV presents the results of the shear layer analyses, most of which are conducted in the local reference frame that characterizes the shear orientation. Finally, the paper is summarized in Sec. V.

II. DIRECT NUMERICAL SIMULATIONS OF HOMOGENEOUS ISOTROPIC TURBULENCE AND MULTI-SCALE RANDOM VELOCITY

The shear layers are studied with DNS databases of incompressible, statistically steady, homogeneous isotropic turbulence. All simulations have used a triply periodic box with the size of L^3, which was discretized by N^3 grid points. The coordinates used in the DNS are denoted by (x, y, z), and the velocity components in these directions are (u, v, w). Pressure and constant density are denoted by p and ρ, respectively. The governing equations are the Navier–Stokes equations for an incompressible fluid. Table I summarizes the parameters of DNS databases, NS1–NS5, which have also been used in Ref. 13. The DNS code is based on a fractional step method, where variables are stored on a staggered grid. The same code has been used in our previous studies.[40–42] Spatial and temporal discretizations are based on the fully conservative 4th-order finite difference scheme[43] and a three-stage and third-order low-storage Runge–Kutta scheme, respectively.

TABLE I. Computational and physical parameters of DNS of forced isotropic turbulence (NS1–NS5), a random velocity field (R3), and decaying turbulence (D1–D3, D2F1, and D2F2).

Run	NS1	NS2	NS3	NS4	NS5	R3	D1	D2	D3	D2F1	D2F2
Flow type	Forced	Forced	Forced	Forced	Forced	Random	Decay	Decay	Decay	Decay	Decay
Initial $E(k)$	$\cdots$	$\cdots$	$\cdots$	$\cdots$	$\cdots$	NS3	NS1	NS2	NS3	NS2	NS2
k_F	$\cdots$	$\cdots$	$\cdots$	$\cdots$	$\cdots$	$\cdots$	$\cdots$	$\cdots$	$\cdots$	$0.05/\eta$	$0.1/\eta$
N	256	512	1024	2048	4096	1024	256	512	1024	512	512
Δ/η	0.83	0.82	0.84	0.82	0.81	0.83	0.88	0.84	0.83	0.81	0.82
Re_L	122	361	1092	2709	5800	946	116	332	946	$\cdots$	$\cdots$
Re_λ	43	72	128	202	296	119	42	71	119	$\cdots$	$\cdots$

The Poisson equation for pressure is solved with the biconjugate gradient stabilized (BiCGStab) method. A statistically steady state is achieved by the linear forcing scheme.[44] Hereafter, an average of a variable is denoted by $\langle * \rangle$, which is taken as a volume average in the entire computational domain and an ensemble average of different snapshots. Table I also presents the spatial resolution Δ divided by the Kolmogorov scale η and the Reynolds numbers based on the integral scale and Taylor microscale, $Re_L = u_0 L_0 / \nu$ and $Re_\lambda = u_0 \lambda / \nu$. Here, the integral scale is calculated as $L_0 = u_0^3 / \varepsilon_0$ with the rms velocity fluctuation $u_0 = \sqrt{(\langle u^2 \rangle + \langle v^2 \rangle + \langle w^2 \rangle)/3}$ and the average of kinetic energy dissipation rate $\varepsilon_0 = \langle 2\nu S_{ij} S_{ij} \rangle$. This estimation of the integral scale is based on the dissipation scaling $\varepsilon_0 = C_\varepsilon (u_0^3 / L_0)$ with a non-dimensional dissipation rate C_ε. Therefore, L_0 can be different from the integral scale defined with an auto-correlation function when C_ε is not constant, for example, turbulence with a low Reynolds number and non-equilibrium turbulence.[45] For turbulence sustained by linear forcing, the integral scale is often calculated in this manner because the ratio between $L_0 = u_0^3 / \varepsilon_0$ and the computational domain size L is determined as the property of the forcing scheme.[44,46–48] The Kolmogorov scale and the Taylor microscale are defined as $\eta = (\nu^3 / \varepsilon_0)^{1/4}$ and $\lambda = \sqrt{15\nu u_0^2 / \varepsilon_0}$, respectively.

The DNS results are compared with a multi-scale, random, and solenoidal velocity field to reveal the kinematic nature of shear layers. Following Ref. 49, velocity vectors in physical space $\boldsymbol{u} = (u, v, w)$ are computed by applying the inverse Fourier transform to velocity vectors in wavenumber space $\hat{\boldsymbol{u}} = (\hat{u}, \hat{v}, \hat{w})$. When $(\hat{u}, \hat{v}, \hat{w})$ is a solenoidal velocity vector, which has a three-dimensional energy spectrum $E(k)$ with random phases, a set of $(\hat{u}, \hat{v}, \hat{w})$ can be calculated as

$$\hat{\boldsymbol{u}}(k_x, k_y, k_z) = \left(\frac{k_y}{k_{xy}} a + \frac{k_x k_z}{k_{xy} k} b, \; \frac{k_y k_z}{k_{xy} k} b - \frac{k_x}{k_{xy}} a, \; -\frac{k_{xy}}{k} b \right) \quad (4)$$

with

$$a = \sqrt{\frac{2E(k)}{4\pi k^2}} e^{i\phi_x} \cos(\phi_z), \quad b = \sqrt{\frac{2E(k)}{4\pi k^2}} e^{i\phi_y} \cos(\phi_z), \quad (5)$$

where $\phi_\alpha(k_x, k_y, k_z)$ ($\alpha = x, y,$ or z) is a random phase between 0 and 2π, (k_x, k_y, k_z) is a wavenumber vector, and k_{xy} and k are $k_{xy} = (k_x^2 + k_y^2)^{1/2}$ and $k = (k_x^2 + k_y^2 + k_z^2)^{1/2}$. Once $E(k)$ is determined with a model spectrum or DNS of turbulence, $(\hat{u}, \hat{v}, \hat{w})$ can be calculated from Eq. (4) with uniform random numbers assigned for ϕ_x, ϕ_y, and ϕ_z. Then, the inverse Fourier transform of $(\hat{u}, \hat{v}, \hat{w})$ yields a random solenoidal velocity profile with the prescribed energy spectrum. Pressure $p(x, y, z)$ is calculated by solving $\nabla^2 p / \rho = \Omega_{ij} \Omega_{ij} - S_{ij} S_{ij}$ with the BiCGStab method. The multi-scale random velocity field is generated by using the energy spectrum calculated in NS3. Here, the three-dimensional energy spectrum in NS3 has been calculated from a one-dimensional one with the assumption of isotropy.[50] The number of the grid points and the domain size used for the random

velocity are the same as in NS3. The parameters of this random velocity field, R3, are shown in Table I. The energy spectrum in NS3 is taken from a single snapshot, while the statistics slightly vary with time. Therefore, Re_L and Re_λ are slightly different between NS3 and R3.

Regions with intense shear have different structures in turbulence and random velocity as shown in Sec. IV. The generation of the shear layers is investigated with DNS of decaying turbulence initialized with the multi-scale random velocity field. Here, DNS is carried out for three initial conditions, which are generated with Eq. (4) by using the energy spectrum in NS1–NS3. These simulations are denoted by D1–D3, respectively. Table I also shows the parameters for D1, D2, and D3 with initial values of Δ/η, Re_L, and Re_λ. The number of grid points and the computational domain size of decaying turbulence are the same as the corresponding DNS of forced isotropic turbulence. A time increment is determined with a constant Courant number of 0.3. The DNS code is the same as the one used for forced isotropic turbulence. Hereafter, the initial values of the integral timescale and Kolmogorov timescale are denoted by $T_{L0} = L_0 / u_0$ and $\tau_{\eta 0} = (\nu / \varepsilon_0)^{1/2}$, which are used to normalize time when the results are presented. In each DNS, time is advanced over $10\tau_{\eta 0}$, which is long enough for the shear layers to develop. The statistics of shear layers are calculated as functions of time with the method presented in Sec. III.

The role of large-scale velocity fluctuations in the formation of shear layers is investigated with DNS of decaying turbulence initialized with a high-pass filtered random velocity field. This velocity field is generated by the inverse Fourier transform of Eq. (4) with a high-pass filtered energy spectrum, $\tilde{E}(k) = G(k)E(k)$ with $G(k) = 1$ for $k \geq k_F$ and $G(k) = 0$ for $k < k_F$. Cases D2F1 and D2F2 are performed for cut-off wavenumbers, $k_F = 0.05/\eta$ and $k_F = 0.1/\eta$, respectively. Here, the original spectrum $E(k)$ in these cases is the same as that in D2. The numerical conditions, such as the number of the grid points, are also the same for D2, D2F1, and D2F2, except for a time increment, which is $(7.5 \times 10^{-4}) T_{L0}$ in D2F1 and D2F2. Because the filter does not change small-scale velocity fluctuations, the Kolmogorov scale is similar for these three cases, as confirmed by the values of Δ/η in Table I. However, the filter significantly decreases the rms velocity fluctuations. Therefore, comparisons of Re_L and Re_λ between the filtered and original cases are not meaningful, and Re_L and Re_λ are not shown in Table I.

III. ANALYSIS OF SHEAR LAYERS WITH THE TRIPLE DECOMPOSITION

A. Triple decomposition of velocity gradient tensor

The triple decomposition of $\nabla \boldsymbol{u}$ is used to detect shear layers from three-dimensional velocity fields.[17] The triple decomposition has to be applied in the basic reference frame. The basic reference frame is different depending on position and time. The triple decomposition considers reference frames obtained with three sequential rotational transformations $\boldsymbol{Q}(\theta_1, \theta_2, \theta_3)$ with angles $0° \leq \theta_1 \leq 180°$, $0° \leq \theta_2 \leq 180°$, and $0° \leq \theta_3 \leq 90°$. The rotational transformation tensor $\boldsymbol{Q}(\theta_1, \theta_2, \theta_3)$ is written as

$$\boldsymbol{Q}(\theta_1, \theta_2, \theta_3) = \begin{pmatrix} \cos\theta_1 \cos\theta_2 \cos\theta_3 - \sin\theta_1 \sin\theta_3 & \sin\theta_1 \cos\theta_2 \cos\theta_3 + \cos\theta_1 \sin\theta_3 & -\sin\theta_2 \cos\theta_3 \\ -\cos\theta_1 \cos\theta_2 \sin\theta_3 - \sin\theta_1 \cos\theta_3 & -\sin\theta_1 \cos\theta_2 \sin\theta_3 + \cos\theta_1 \cos\theta_3 & \sin\theta_2 \sin\theta_3 \\ \cos\theta_1 \sin\theta_2 & \sin\theta_1 \sin\theta_2 & \cos\theta_2 \end{pmatrix}. \quad (6)$$

The velocity gradient tensor in a rotated reference frame is calculated as $(\nabla\boldsymbol{u})^* = \boldsymbol{Q}(\nabla\boldsymbol{u})\boldsymbol{Q}^T$, where superscript $*$ represents a tensor evaluated in the rotated reference frame. The triple decomposition considers the following decomposition:

$$(\nabla\boldsymbol{u}_{RES})^*_{ij} = \mathrm{sgn}\left[(\nabla\boldsymbol{u})^*_{ij}\right]\min\left[|(\nabla\boldsymbol{u})^*_{ij}|, |(\nabla\boldsymbol{u})^*_{ji}|\right], \quad (7)$$

$$(\nabla\boldsymbol{u}_S)^*_{ij} = (\nabla\boldsymbol{u})^*_{ij} - (\nabla\boldsymbol{u}_{RES})^*_{ij} \quad (8)$$

for $i, j = 1, 2, 3$. The decomposition has to be applied in the basic reference frame, where shearing motion is effectively extracted with Eqs. (7) and (8). For a tensor A_{ij}, the norm can be defined as $||A|| = \sqrt{A_{ij}A_{ij}}$. When Eqs. (7) and (8) are applied, the norm of the velocity gradient tensor is also decomposed as

$$||(\nabla\boldsymbol{u})^*||^2 = ||(\nabla\boldsymbol{u}_{RES})^*||^2 + 4I^*, \quad (9)$$

$$I^* \equiv |\Omega^*_{12}S^*_{12}| + |\Omega^*_{23}S^*_{23}| + |\Omega^*_{31}S^*_{31}|, \quad (10)$$

where I^* is called an interaction scalar.[17] The basic reference frame is determined with I^*, which is different depending on the reference frames. The basic reference frame assumes that I^* is the largest among all the possible reference frames defined with Eq. (6). The largest I^* indicates that the effective shear component of $(\nabla\boldsymbol{u})^*$ is fully extracted by Eqs. (7) and (8). The procedure developed in Ref. 51 is used to identify the basic reference frame from many reference frames defined with discrete sets of $(\theta_1, \theta_2, \theta_3)$, where the angles are changed by $\Delta\theta$. First, this procedure examines the reference frames given by all sets of $(\theta_1, \theta_2, \theta_3)$ for

$$\theta_1 = 0, 45°, 90°, ..., 180°,$$
$$\theta_2 = 0, 45°, 90°, ..., 180°, \quad (11)$$
$$\theta_3 = 0, 45°, 90°,$$

where the angles are discretely changed by $\Delta\theta = 45°$. I^* calculated for all reference frames provides $(\theta_1, \theta_2, \theta_3)$, which gives the largest I^* among the reference frames considered for Eq. (11). These angles with the largest I^* are denoted by $(\theta_1^{(1)}, \theta_2^{(1)}, \theta_3^{(1)})$. Then, the largest I^* is again searched for the reference frames defined with the following angles:

$$\theta_1 = \theta_1^{(1)} - 45°/2, \quad \theta_1^{(1)} - 45°/2 + 15°, ..., \theta_1^{(1)} + 45°/2,$$
$$\theta_2 = \theta_2^{(1)} - 45°/2, \quad \theta_2^{(1)} - 45°/2 + 15°, ..., \theta_2^{(1)} + 45°/2, \quad (12)$$
$$\theta_3 = \theta_3^{(1)} - 45°/2, \quad \theta_3^{(1)} - 45°/2 + 15°, ..., \theta_3^{(1)} + 45°/2,$$

with $\Delta\theta = 15°$. The angles for the largest I^* are denoted by $(\theta_1^{(2)}, \theta_2^{(2)}, \theta_3^{(2)})$. Finally, the same procedure to find the largest I^* is repeated for the angles given by

$$\theta_1 = \theta_1^{(2)} - 15°/2, \quad \theta_1^{(2)} - 15°/2 + 5°, ..., \theta_1^{(2)} + 15°/2,$$
$$\theta_2 = \theta_2^{(2)} - 15°/2, \quad \theta_2^{(2)} - 15°/2 + 5°, ..., \theta_2^{(2)} + 15°/2, \quad (13)$$
$$\theta_3 = \theta_3^{(2)} - 15°/2, \quad \theta_3^{(2)} - 15°/2 + 5°, ..., \theta_3^{(2)} + 15°/2,$$

with $\Delta\theta = 5°$, which is small enough to accurately identify the basic reference frame.[14,29] The set of $(\theta_1, \theta_2, \theta_3)$ that yields the largest I^* for Eq. (13) is used to define the basic reference frame, and these angles are denoted by $(\theta_1^B, \theta_2^B, \theta_3^B)$. Variables evaluated in the basic reference frame are denoted with a superscript B, for example, $(\nabla\boldsymbol{u}_S)^B$. In the basic reference frame, the shear tensor $(\nabla\boldsymbol{u}_S)^B$ is extracted from

$(\nabla\boldsymbol{u})^B$ with Eqs. (7) and (8). The other components, $(\nabla\boldsymbol{u}_E)^B$ and $(\nabla\boldsymbol{u}_R)^B$, in the basic reference frame are obtained from the residual tensor as

$$(\nabla\boldsymbol{u}_E)^B_{ij} = \left[(\nabla\boldsymbol{u}_{RES})^B_{ij} + (\nabla\boldsymbol{u}_{RES})^B_{ji}\right]/2, \quad (14)$$

$$(\nabla\boldsymbol{u}_R)^B_{ij} = \left[(\nabla\boldsymbol{u}_{RES})^B_{ij} - (\nabla\boldsymbol{u}_{RES})^B_{ji}\right]/2. \quad (15)$$

Finally, $\nabla\boldsymbol{u}_S$, $\nabla\boldsymbol{u}_R$, and $\nabla\boldsymbol{u}_E$ in the reference frame of DNS are obtained respectively from $(\nabla\boldsymbol{u}_S)^B$, $(\nabla\boldsymbol{u}_R)^B$, and $(\nabla\boldsymbol{u}_E)^B$ by applying the inverse coordinate transformation of $\boldsymbol{Q}(\theta_1^B, \theta_2^B, \theta_3^B)$.

B. Conditional averages of shear layers

The shear layers can be identified in the three-dimensional profile of I_S.[29] The statistical properties of shear layers are evaluated with the procedure developed in Ref. 13. The flow around the local maxima of I_S is examined because the shear layer structures identified with I_S have a local peak of I_S. The local maxima of I_S can be detected with the Hessian matrix of I_S. A shear coordinate $(\zeta_1, \zeta_2, \zeta_3)$ is introduced at the location of each local maximum, which is the origin of $(\zeta_1, \zeta_2, \zeta_3)$. Hereafter, the velocity vector in the shear coordinate is denoted by $(u_{\zeta_1}, u_{\zeta_2}, u_{\zeta_3})$. This coordinate assumes that ζ_1 is given by the vorticity vector of shear, $(\boldsymbol{\omega}_S)_i = \epsilon_{ijk}(\nabla\boldsymbol{u}_S)_{jk}$, where ϵ_{ijk} is the Levi-Civita symbol and that $\partial u_{\zeta_3}/\partial\zeta_2$ has the largest contribution to the shear. The directions of $(\zeta_1, \zeta_2, \zeta_3)$ are determined by finding the reference frame where $\partial u_{\zeta_3}/\partial\zeta_2$ is the largest among all possible reference frames under the condition that the ζ_1 direction is given by $\boldsymbol{\omega}_S/|\boldsymbol{\omega}_S|$. The procedure to obtain the directions of $(\zeta_1, \zeta_2, \zeta_3)$ is presented in Ref. 51. Once the shear coordinate is identified, variables defined on the DNS grid are interpolated on the shear coordinate with a third-order Lagrange polynomial interpolation scheme, where the shear coordinate is discretized with a spacing smaller than the Kolmogorov scale. The interpolation is applied repeatedly for the shear coordinates defined at all detected local maxima of I_S, for which ensemble averages of variables are conditionally taken as functions of $(\zeta_1, \zeta_2, \zeta_3)$. The average taken in the shear coordinate is denoted with an overbar, for example, $\overline{I_S}(\zeta_1, \zeta_2, \zeta_3)$.

The present analysis of the shear layers is motivated by the studies of turbulent/non-turbulent interface (TNTI), which forms between turbulent and non-turbulent regions in intermittent turbulent flows, such as jets,[31,32,52,53] mixing layers,[54–56] wakes,[30,57] and boundary layers.[58,59] These studies of TNTI combine the detection method of the TNTI with averages taken in a local coordinate system.[30] The origin of the local coordinate is located at the interface, and the orientation of the one-dimensional coordinate is often taken in the normal direction of the interface. Then, ensemble averages of samples obtained for different locations on the TNTI are conditionally taken as functions of the position in the local coordinate. Similarly, the present study defines the shear coordinates for each detected shear layer and takes ensemble averages of all shear layers as functions of the positions in the shear coordinate.

IV. RESULTS AND DISCUSSION

A. Fundamental characteristics of shear layers

Figure 3 shows isosurfaces of I_S (white) and I_R (orange), which are used to visualize shear layers and vortex tubes, respectively. Here, the isosurface values are determined based on the Kolmogorov
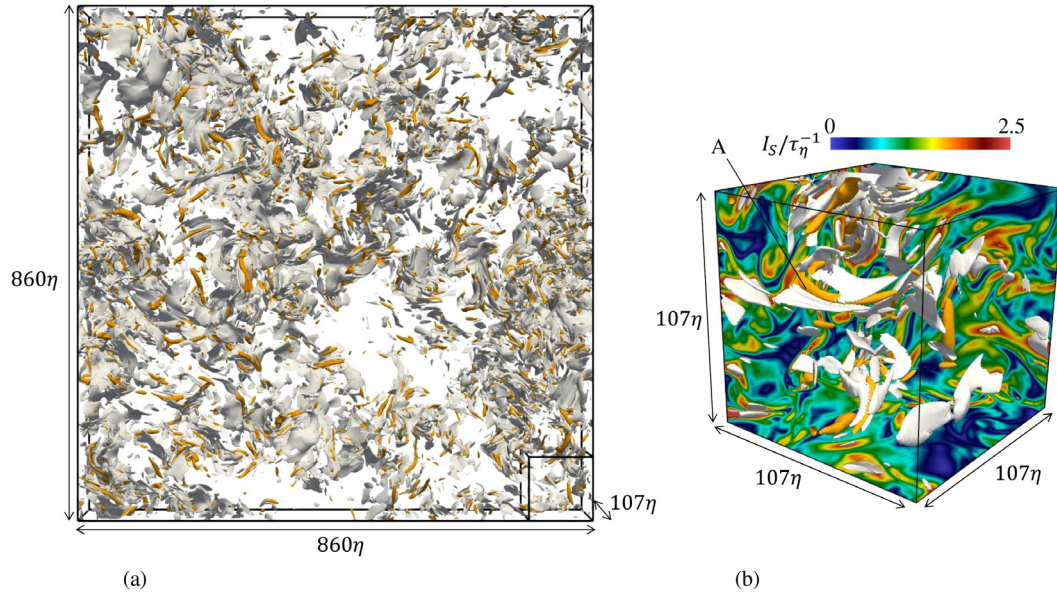
FIG. 3. Visualization of small-scale structures in NS3: shear layers (white) and vortex tubes (orange) are visualized with isosurfaces of shear intensity ($I_S/\tau_\eta^{-1} = 2$) and rotation intensity ($I_R/\tau_\eta^{-1} = 1.5$), respectively. Panel (b) shows the close-up of the right bottom corner of the visualized domain in (a). The color contour of I_S in panel (b) is shown on the surfaces of the small cubic domain with the size of $(107\eta)^3$.

timescale $\tau_\eta = (\nu/\varepsilon_0)^{1/2}$. The isosurface of I_S has a flat shape and successfully detects the thin layer structures with shearing motion. Figure 3(a) suggests that the number density of shear layers is not uniform in space: there are regions where more shear layers are found than in other regions. For example, the upper half on the left of the visualized domain contains many shear layers, while there is a void region with only a few shear layers near the center of the domain. The number density of shear layers seems to be correlated with that of vortex tubes. The intermittent distribution of vortex-tube clusters has been pointed out in previous DNS studies.[60,61] The vortex marked as A in Fig. 3(b) is surrounded by two shear layers. As also confirmed from the temporal evolution of shear layers and vortices,[13] we can consider that this vortex is being generated by the roll-up of a single shear layer, which is being split into two shear layers. This configuration of the shear layers and the vortex is consistent with a spiral vortex sheet.[15] Previous studies of shear layers have shown that the number of vortex tubes wrapped by shear layers is not large and many shear layers have a flat shape.[13,16,51,62,63] Therefore, the statistics obtained for all shear layers may not represent the characteristics of the spiral shear layers.

Figure 4 compares two-dimensional profiles of u, I_S, and I_R between NS3 and R3. Flow structures identified in these figures are different between NS3 and R3 although both flows have the same energy spectrum. Flat layer structures with large I_S do not appear in the random velocity, where small spots of large I_S are found. When vortex tubes with large I_R are parallel to the visualized plane, they appear with an elongated shape in the axial direction of the vortices. These patterns are found in NS3 but not in R3. These observations suggest that the random velocity does not possess flow structures of shear layers and vortex tubes although motions of shear and rotation can be locally significant.

Before the main results of the shear layer analysis are presented, we shortly discuss the mean flow profile around the shear

layers[13] because the mean flow topology is found to be important in the transport of kinetic energy as discussed below. Figure 5 shows the mean velocity vectors $(\overline{u_{\zeta_1}}, \overline{u_{\zeta_2}}, \overline{u_{\zeta_3}})$ and the mean shear intensity $\overline{I_S}$ calculated as functions of the shear coordinate $(\zeta_1, \zeta_2, \zeta_3)$ with the ensemble averages taken for all local maxima of I_S. Here, the results are presented for two-dimensional planes that cross the center of the shear layer. In the shear coordinate, the shear is expressed by $\partial u_{\zeta_3}/\partial \zeta_2$. The shear layer with large $\overline{I_S}$ is found between the flows in the $\pm \zeta_3$ directions around the center of Fig. 5(b). Figure 5(a) indicates that the shear layer is subject to a biaxial strain with stretching in the ζ_1 direction and compression in the ζ_2 direction. The shear layer with large $\overline{I_S}$ is thin in the ζ_2 direction and the thickness scales with the Kolmogorov scale.[13,14] In Fig. 5(c), $\overline{I_S}$ gradually decreases with a distance from the center. This is because the shear layers often have a curved shape as visualized in Fig. 3 and the averaging procedure applied at large $|\zeta_1|$ or large $|\zeta_3|$ mixes the samples taken from both inside and outside the shear layer even on the ζ_1 and ζ_3 axes.

A similar analysis based on a local coordinate system has been carried out in previous studies. A coordinate system defined with the eigenvectors of the rate-of-strain tensor S_{ij}, called a strain eigenframe, has been used in Refs. 64 and 65. Because S_{ij} can be decomposed as $S_{ij} = (S_S)_{ij} + (\nabla u_E)_{ij}$ with $(S_S)_{ij} = [(\nabla u_S)_{ij} + (\nabla u_S)_{ji}]/2$, the eigenvectors of S_{ij} are related to the shear coordinate considered in this study. Therefore, a similar flow topology has been observed in the mean velocity field taken in the strain eigenframe and the shear coordinate although the analysis of the strain eigenframe has been conducted without identifying the shear layers.[13,64] This is because $(S_S)_{ij}$ has a greater contribution to S_{ij} than $(\nabla u_E)_{ij}$ in most regions in turbulence and the statistics in an entire flow field are significantly influenced by shearing motion.[13,29]

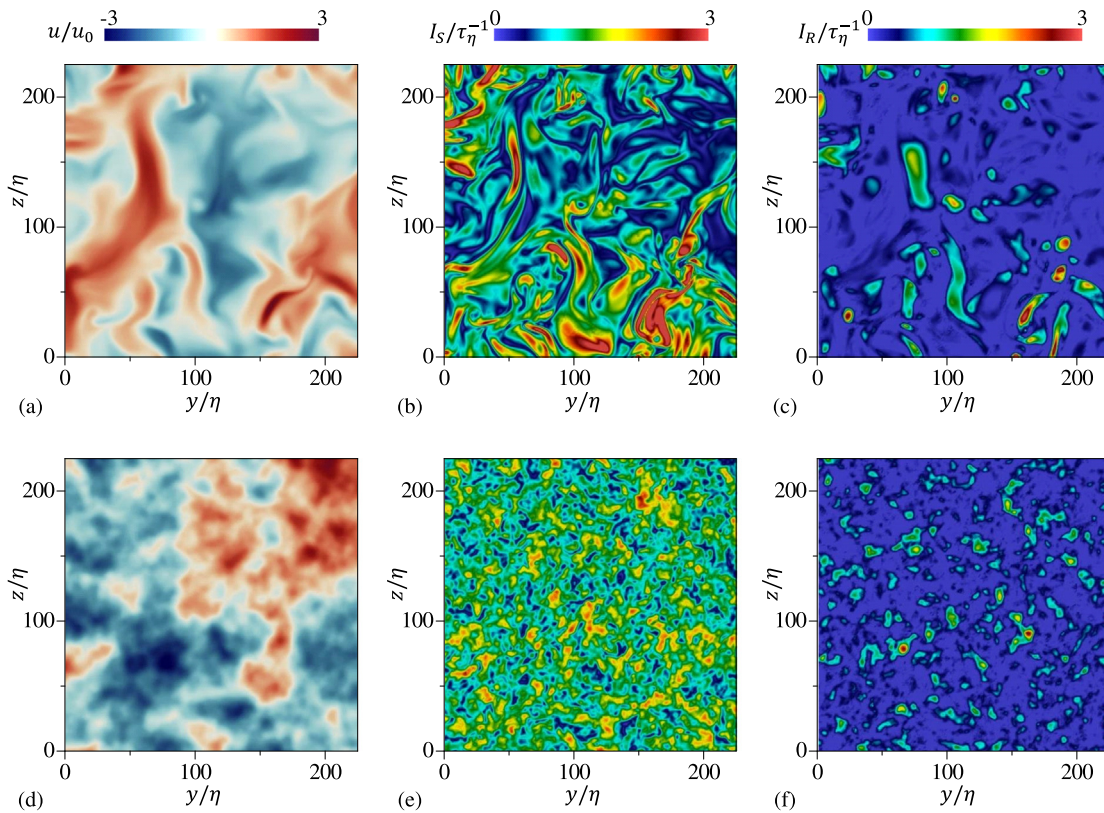**FIG. 4.** Two-dimensional profiles of (a) and (d) velocity u, (b) and (e) shear intensity I_S, and (c) and (f) rotation intensity I_R on a y–z plane in (a)–(c) NS3 and (d)–(f) R3. Only a small part of the domain is shown in the figure.

Figure 6 shows the profiles of the mean velocity vectors and $\overline{I_S}$ in the random velocity field. The mean velocity on the ζ_1–ζ_2 and ζ_1–ζ_3 planes is negligibly small, and the velocity vectors are shown only in Fig. 6(b), where the flows in the $\pm\zeta_3$ directions are observed around the center of the shear layer. The shape of the shear layer is different between turbulence and the random velocity field. The shear layer in R3 is small in the ζ_1 and ζ_3 directions than that in NS3 shown in Fig. 5. This observation in the mean flow field is also consistent with flow visualization in Fig. 4, where the thin shear layers are not found in the random velocity field.
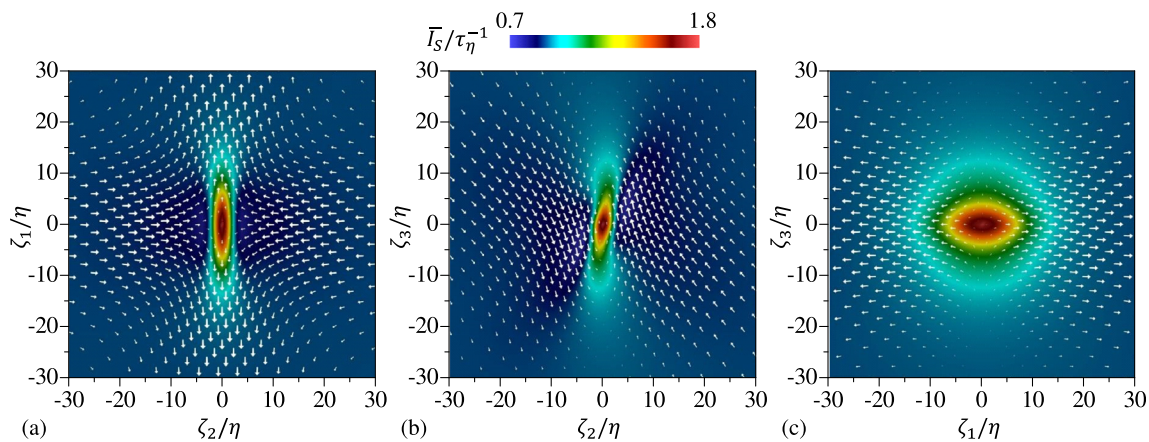

FIG. 5. Mean shear intensity $\overline{I_S}$ and mean velocity vectors $(\overline{u_{\zeta_1}}, \overline{u_{\zeta_2}}, \overline{u_{\zeta_3}},)$ near shear layers in NS3: (a) ζ_1–ζ_2 plane at $\zeta_3 = 0$; (b) ζ_2–ζ_3 plane at $\zeta_1 = 0$; (c) ζ_1–ζ_3 plane at $\zeta_2 = 0$. The length of vectors represents the vector magnitude.
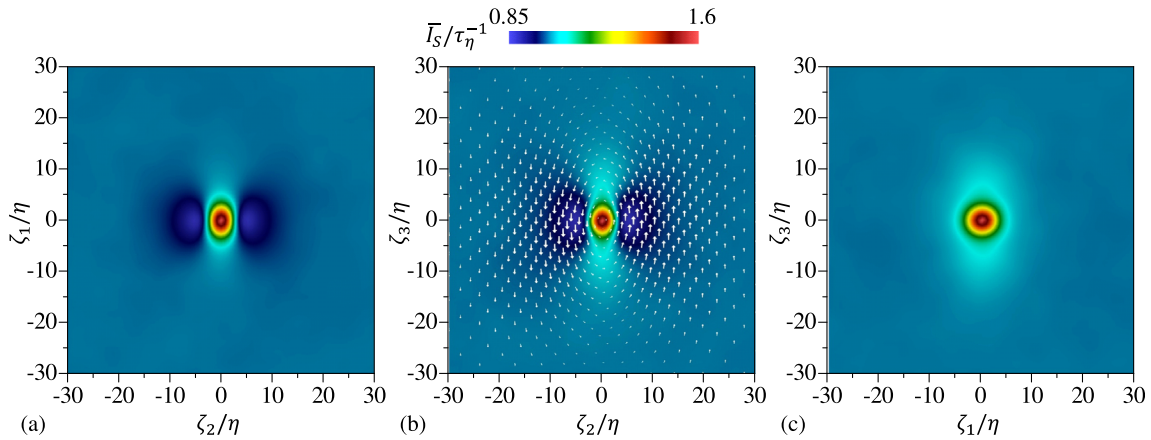
FIG. 6. The same as in Fig. 5 but for random velocity R3: (a) ζ_1–ζ_2 plane at $\zeta_3 = 0$; (b) ζ_2–ζ_3 plane at $\zeta_1 = 0$; (c) ζ_1–ζ_3 plane at $\zeta_2 = 0$. The mean velocity vectors are not shown in (a) and (c) because the mean velocity is almost zero in these planes.

B. Configuration of vortex tubes near shear layers

The relation between motions of shear and rotation is investigated around the shear layers. Figure 7 shows the average of I_R around the shear layers on the ζ_2–ζ_3 plane at $\zeta_1 = 0$ for NS3, NS5, and R3. The white dotted line is an isoline of $\overline{I_S}$ and marks the location of the shear layer. The direction of vortex tubes can be assessed with a vorticity vector defined with $\nabla \boldsymbol{u}_R$ as $(\boldsymbol{\omega}_R)_i = \epsilon_{ijk}(\nabla \boldsymbol{u}_R)_{jk}$. The three components of $\boldsymbol{\omega}_R$ in the shear coordinate system are denoted by $(\boldsymbol{\omega}_R)_{\zeta_1}$, $(\boldsymbol{\omega}_R)_{\zeta_2}$, and $(\boldsymbol{\omega}_R)_{\zeta_3}$. Figure 7 also shows isolines of positive and negative $\overline{(\boldsymbol{\omega}_R)_{\zeta_1}}$. Four nearly circular regions with large $\overline{I_R}$ can be identified near the shear layer: two of them have large $\overline{I_R}$ with $\overline{(\boldsymbol{\omega}_R)_{\zeta_1}} < 0$ on both sides of the shear layer; the others are located in the shear layer and have large $\overline{I_R}$ with $\overline{(\boldsymbol{\omega}_R)_{\zeta_1}} > 0$. A similar configuration of rotating motions near the shear layer is also observed for R3. Therefore, rotating motions near the shear layer arise from the kinematic nature of a multi-scale random velocity field, which is free from the dynamics of

Navier–Stokes equations. Although shear layers are observed in the vicinity of vortex tubes,[15] this configuration of vortices is not attributed solely to the dynamics of the Navier–Stokes equations. For R3, the center of rotating motion with $\overline{(\boldsymbol{\omega}_R)_{\zeta_1}} < 0$ (white lines) appears at $\zeta_3 = 0$, and the profile of $\overline{I_R}$ is symmetric with respect to $\zeta_2 = 0$. However, this symmetry is not found for NS3 and NS5 as the center of large $\overline{I_R}$ on the sides of the shear layer appears in the first and third quadrants of (ζ_2, ζ_3). It will be shown that the tilted shear layer with rotating motions is important in the formation of the biaxial strain acting on the shear layer.

Figure 8(a) presents a sketch of the flow associated with the shear layer and vortices. It seems that the vortices with $\overline{(\boldsymbol{\omega}_R)_{\zeta_1}} < 0$ on sides of the shear layer induce the flow in the $\pm \zeta_3$ directions that contributes to the shear with $\partial u_{\zeta_3}/\partial \zeta_2 > 0$ and the compressive strain with $\partial u_2/\partial \zeta_2 < 0$. The vorticity vector due to the shear $(\boldsymbol{\omega}_S)_i = \epsilon_{ijk}(\nabla \boldsymbol{u}_S)_{jk}$ is oriented in the same direction as the vortices (shown in red) found inside the shear layer because both $\overline{(\boldsymbol{\omega}_R)_{\zeta_1}}$ and $\overline{(\boldsymbol{\omega}_S)_{\zeta_1}} \approx \overline{\partial u_{\zeta_3}/\partial \zeta_2}$ are
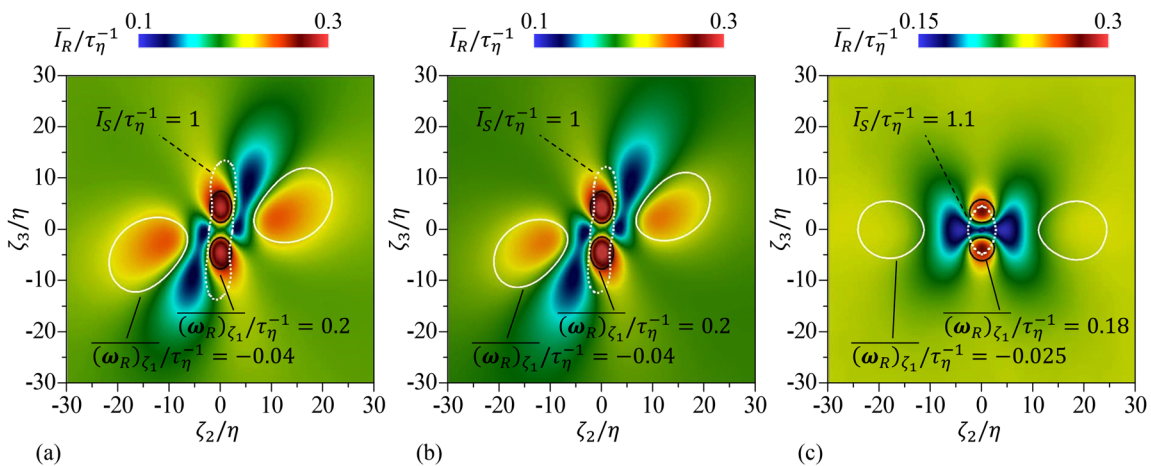
FIG. 7. Mean intensity of rotation $\overline{I_R}$ on the ζ_2–ζ_3 plane at $\zeta_1 = 0$ in (a) NS3, (b) NS5, and (c) R3. The dotted and solid lines represent the isolines of $\overline{I_S}$ and $\overline{(\boldsymbol{\omega}_R)_{\zeta_1}}$, where $(\boldsymbol{\omega}_R)_{\zeta_1}$ is the ζ_1 component of the vorticity vector of $\nabla \boldsymbol{u}_R$.
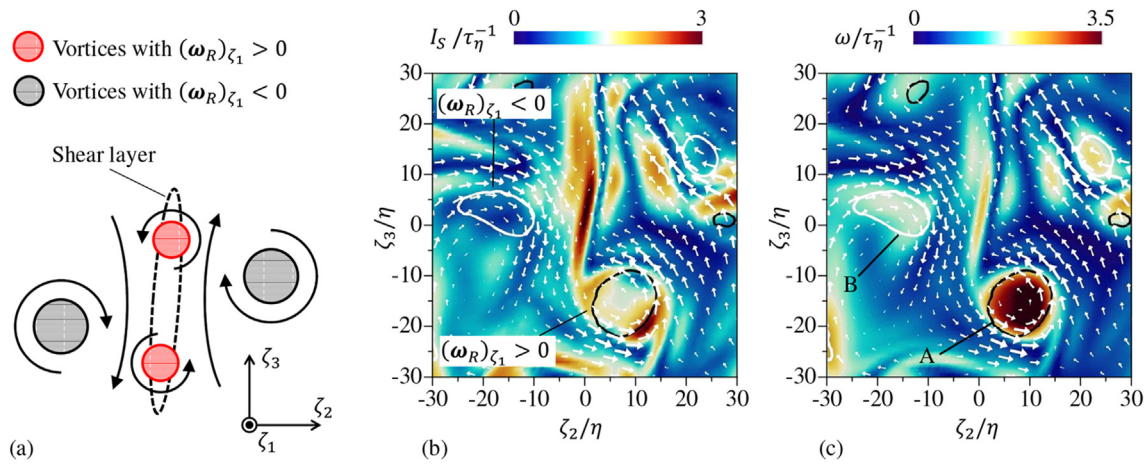
FIG. 8. (a) Sketch of the vortices observed in the averaged flow field near the shear layer. (b) and (c) Visualization of a shear layer in the two-dimensional shear coordinate (ζ_2, ζ_3) at $\zeta_1 = 0$ with color contours of (b) shear intensity I_S and (c) vorticity magnitude ω. Velocity vectors relative to the velocity at $(\zeta_1, \zeta_2, \zeta_3) = (0, 0, 0)$ are also shown in both panels. White and black lines are the isolines of $(\omega_R)_{\zeta_1}/\tau_\eta^{-1} = -0.8$ and 0.8, respectively.

positive. Each shear layer is not always surrounded by all of the four vortices found in the mean flow field. The vortex with $(\omega_R)_{\zeta_1} < 0$ often appears only on one side of the shear layer for either $\zeta_2 > 0$ or $\zeta_2 < 0$. The average taken for all shear layers results in large $\overline{I_R}$ on both sides of the shear layer in Fig. 7. For the same reason, two vortices with $(\omega_R)_{\zeta_1} > 0$ may not always appear within a single shear layer. However, a similar configuration of a shear layer and vortices with negative $(\omega_R)_{\zeta_1}$ is found even in an instantaneous flow field. Figures 8(b) and 8(c) visualize a shear layer in the shear coordinate system with a color contour of I_S or ω and isolines of $(\omega_R)_{\zeta_1}$ on the ζ_2–ζ_3 plane. The center of Fig. 8(b) has large I_S in a thin layer structure. On the left of the shear layer, there is a circular region with $(\omega_R)_{\zeta_1} < 0$ (B). The rotating fluid motion caused by this vortex contributes to the flow in the $-\zeta_3$ direction on the left of the shear layer. The mean profile of I_R in Fig. 7 agrees between NS3 and NS5 when the shear coordinate is normalized by the Kolmogorov scale. This indicates that the vortices near the shear layer are small-scale structures. Typical small-scale vortex tubes have a diameter of about 10η.[7–11] The diameter of vortices is close to 10η in the instantaneous flow field in Fig. 8. In Figs. 7(a) and 7(b), the region with large $\overline{I_R}$ on each side of the shear layer (white lines) has a slightly larger size than 10η. This can be caused by the variation of the vortex position, whose distance from the shear layer is not constant.

In Figs. 8(b) and 8(c), one can also find another circular region with $(\omega_R)_{\zeta_1} > 0$ below the shear layer (marked as A). The vorticity profile around the shear layer is similar to that in the Kelvin–Helmholtz instability,[66,67] and the vortex with $(\omega_R)_{\zeta_1} > 0$ below the shear layer is generated by the roll-up of the shear layer. The shear layer visualized in Figs. 8(b) and 8(c) is chosen to discuss the shear instability although many shear layers do not appear along with the nearby vortices arising from the instability. Therefore, Figs. 8(b) and 8(c) do not represent a common flow field around shear layers, which is better appreciated by the statistics calculated with many shear layers. One may consider that large $\overline{I_R}$ with $\overline{(\omega_R)_{\zeta_1}} > 0$ in Fig. 7 is associated with the vortex tube that has been generated or is being generated by the instability of the shear layer. However, the

rotating motion with $\overline{(\omega_R)_{\zeta_1}} > 0$ is also seen in R3, where the flow field is independent of the instability that is the dynamical consequence of the Navier–Stokes equations. Therefore, this configuration of shear and rotation is not caused by the instability of shear layers.

When two vortex tubes with the same vorticity direction appear close to each other, a large velocity gradient can be observed between them. Thus, a pair of vortex tubes may generate an intense shear layer in turbulent flows. However, flow visualization in Figs. 3, 8(b), and 8(c) suggests that the shear layers are not always surrounded by two vortices. As also discussed below with the kinetic energy budget, the present results imply that at least one vortex tube is related to the generation of shear layers. Numerical studies of shear layers (vortex sheets) have observed that when the shear instability generates two vortex tubes, a strained shear layer with compression in the normal direction of the shear layer forms between the vortex tubes.[68,69] The local flow topology around the strained shear layer is similar to the mean velocity field observed near the shear layers in Fig. 5. It has also been shown that two vortex tubes on the sides of the strained shear layer can merge to form a larger vortex tube. A similar paring of vortex tubes may also occur near the shear layers in turbulent flows.

In Fig. 7, the vortex with $(\omega_R)_{\zeta_1} < 0$ is separated from the shear layer. Their separation is quantified from the two-dimensional profile of $\overline{I_R}$ as the distance of the local maxima of $\overline{I_R}$ with $(\omega_R)_{\zeta_1} < 0$ from $(\zeta_2, \zeta_3) = (0, 0)$. Figure 9 plots this distance δ_{RS} normalized by η, λ, or L_0 against Re_λ. As Re_λ increases, δ_{RS}/λ and δ_{RS}/L_0 becomes small. On the other hand, $\delta_{RS}/\eta \approx 12$ hardly depends on Re_λ. Thus, the configuration of the vortices near shear layers is characterized by the Kolmogorov scale. These shear layers and vortices are separated and not connected. In Figs. 7(a) and 7(b), there are regions with small $\overline{I_R}$ between the vortices with $(\omega_R)_{\zeta_1} < 0$ and the shear layer. These regions with small $\overline{I_R}$ also have small $\overline{I_S}$ in Fig. 5(b) and belong to neither the vortices nor the shear layer. As shown below, these regions between shear layers and vortex tubes are occupied with a flow with large kinetic energy, which contributes to shearing motion.
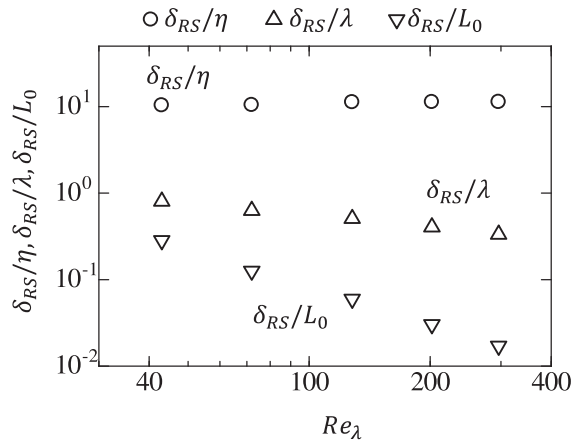
FIG. 9. Re_λ dependence of the distance δ_{RS} between $(\zeta_2, \zeta_3) = (0,0)$ and the local maxima of $\overline{I_R}$ with $\overline{(\omega_R)}_{\zeta_1} < 0$. Here, δ_{RS} is normalized by the Kolmogorov scale η, Taylor microscale λ, or integral scale L_0.

C. The kinetic energy budget near the shear layers

The kinetic energy budget around the shear layer is evaluated to investigate the mechanism that sustains the shearing motion around the shear layer. Figure 10 shows the mean profile of the turbulent kinetic energy $\bar{k} = \overline{(u^2 + v^2 + w^2)/2}$ near the shear layer. The dotted line and solid lines are the isolines of $\overline{I_S}$ and $\overline{(\omega_R)}_{\zeta_1}$, respectively. Figures 10(a) and 10(b) indicate that the shear layer has small $\bar{k}$ and forms between large-$\bar{k}$ regions. In Fig. 10(b), large $\bar{k}$ appears between the vortices with $\overline{(\omega_R)}_{\zeta_1} < 0$ and the shear layer, implying that shear layers are formed by the energetic fluid motion induced by nearby vortices as also confirmed in the instantaneous flow field in Fig. 8. Figure 10(c) shows $\bar{k}$ on the shear-layer parallel plane. The low-$\bar{k}$ region is extended in the ζ_3 direction. A comparison between Figs. 5 and 10 indicates that the kinetic energy distribution is related to the mean velocity profile around the shear layer. For example, the mean velocity

is small for a wide range of ζ_3 at $(\zeta_1, \zeta_2) = (0,0)$, where small $\bar{k}$ is found. Furthermore, large values of $\bar{k}$ in Fig. 10(b) are found on both sides of the shear layer, where the mean velocity due to the shear, $\overline{u_{\zeta_3}}$, is large. The large mean velocity of the biaxial strain, $(\overline{u_{\zeta_1}}, \overline{u_{\zeta_2}})$, in Fig. 5(a) is also correlated with the profile of $\bar{k}$ in Fig. 10(a). Thus, the turbulent kinetic energy around the shear layer is dominated by the mean flow around the shear layer, which consists of the shear and the biaxial strain. Figure 11 shows the results for R3. Large $\bar{k}$ between the shear layer and the vortices with $\overline{(\omega_R)}_{\zeta_1} < 0$ is similar to that for NS3. However, the random velocity field does not have the biaxial strain around the shear layer. Therefore, large $\bar{k}$ associated with the strain field cannot be seen for R3. For this reason, $\bar{k}$ on the ζ_1–ζ_2 plane decreases at large $|\zeta_1|$ and $|\zeta_2|$ in Fig. 11(a).

The transport equation for turbulent kinetic energy k is written as

$$\frac{\partial k}{\partial t} + u_j \frac{\partial k}{\partial x_j} = -\frac{1}{\rho}\frac{\partial u_j p}{\partial x_j} - \frac{\partial}{\partial x_j}(-2\nu u_i S_{ij}) - 2\nu S_{ij}S_{ij} + u_j f_j, \quad (16)$$

where f_i is the forcing term. The reference frame moving with the shear layer (X, Y, Z) is introduced to eliminate the effects of the sweeping motion of shear layers on the advection term. For each detected shear layer, the fluid at the shear layer center is advected by the velocity at $(\zeta_1, \zeta_2, \zeta_3) = (0, 0, 0)$, which is denoted by $\boldsymbol{u}_0$. Once the transformation from (x, y, z) to the reference frame moving with $\boldsymbol{u}_0$ is applied, the advection term in the moving reference frame is expressed as $[u_j - (\boldsymbol{u}_0)_j](\partial k/\partial x_j)$. More details of the coordinate transformation to the local moving reference frame can be found in Refs. 70 and 71. The following transport equation is defined for each detected shear layer in the moving reference frame:

$$\frac{\partial k}{\partial t} = -\underbrace{\left[u_j - (\boldsymbol{u}_0)_j\right]\frac{\partial k}{\partial x_j}}_{T_k} - \underbrace{\frac{1}{\rho}\frac{\partial u_j p}{\partial x_j}}_{P_k} - \underbrace{\frac{\partial}{\partial x_j}(-2\nu u_i S_{ij})}_{D_k} \underbrace{-2\nu S_{ij}S_{ij}}_{\varepsilon_k} \underbrace{+u_j f_j}_{F_k},$$

$$(17)$$

where T_k is the advection term, P_k is the pressure diffusion term, D_k is the viscous diffusion term, ε_k is the dissipation term, and F_k is the
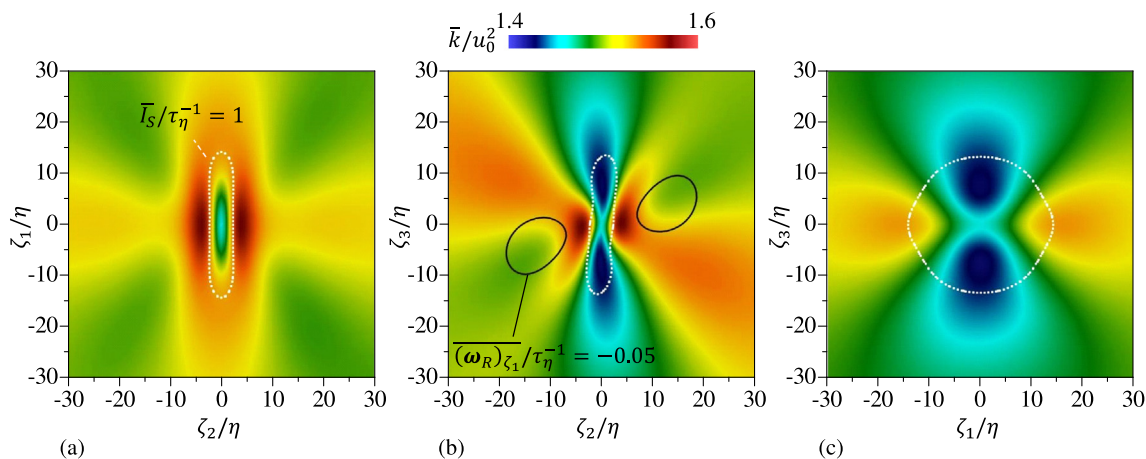

FIG. 10. Averaged turbulent kinetic energy $\bar{k}$ near the shear layers in NS3: (a) ζ_1–ζ_2 plane at $\zeta_3 = 0$; (b) ζ_2–ζ_3 plane at $\zeta_1 = 0$; (c) ζ_1–ζ_3 plane at $\zeta_2 = 0$. The dotted line represents the isoline of $\overline{I_S}$. Panel (b) also shows the isolines of $\overline{(\omega_R)}_{\zeta_1}$ (black lines).
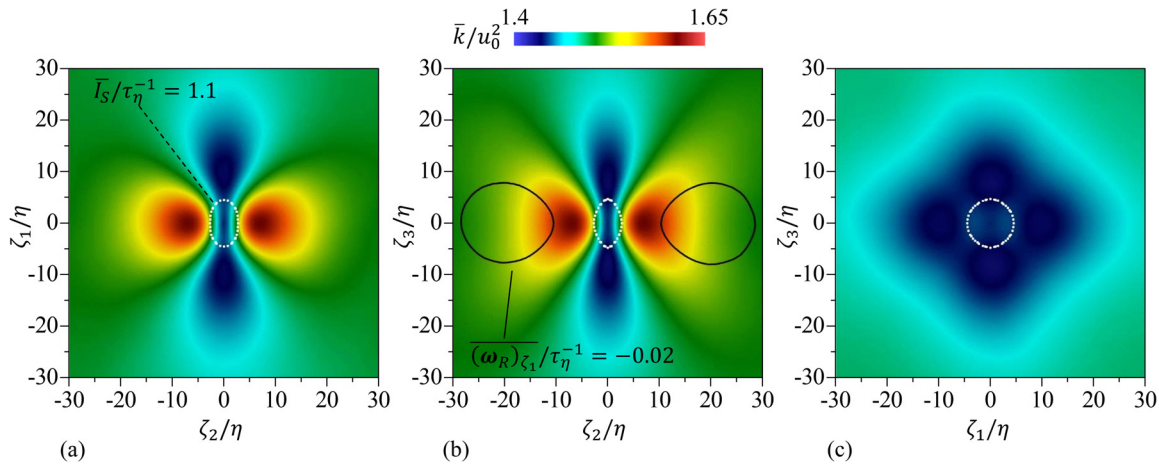
FIG. 11. The same as in Fig. 10 but for random velocity (R3): (a) ζ_1–ζ_2 plane at $\zeta_3 = 0$; (b) ζ_2–ζ_3 plane at $\zeta_1 = 0$; (c) ζ_1–ζ_3 plane at $\zeta_2 = 0$.

production term due to the external force. The spatial derivative is written in the form of $\partial/\partial x_i$ because of $\partial/\partial x_i = \partial/\partial X_i$.[70] These terms are evaluated on the shear coordinate $(\zeta_1, \zeta_2, \zeta_3)$ for each local maximum location of I_S. The ensemble average of each term is taken to assess the turbulent kinetic energy budget around the shear layer.

Figure 12 plots the profiles of the averaged terms along the ζ_2 axis at $(\zeta_1, \zeta_3) = (0, 0)$ in NS3. For the linear forcing scheme, F_k is proportional to the turbulent kinetic energy k. However, the energy input by the forcing term only weakly depends on ζ_2 and the spatial variation of F_k is not significant compared with the other terms. The dissipation $\overline{\varepsilon_k}$ becomes large within the shear layer as expected from the large velocity gradient inside the shear layer and the fractal dimension analysis.[60] All the spatial transport terms contribute to the energy transfer from the outside to the inside of the shear layer. Pressure and viscous diffusion terms, $\overline{P_k}$ and $\overline{D_k}$, are positive in the shear layer and change the sign outside the shear layer, and thus, the energy is transferred toward the center of the shear layer, where the energy dissipation is active. The advection term contributes to the energy transfer to the vicinity of the shear layer.
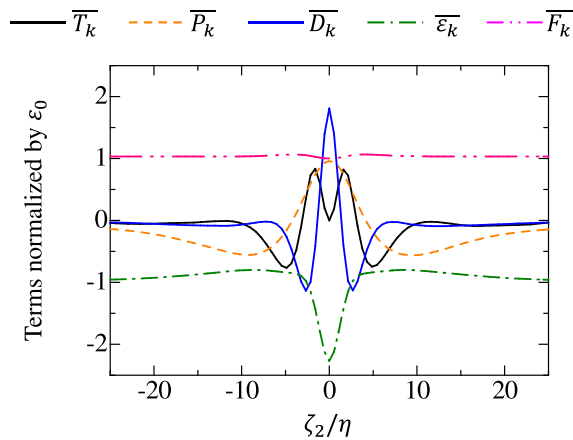

FIG. 12. Averages of the transport equation of turbulent kinetic energy near shear layers in NS3. The results are presented along ζ_2 axis at $(\zeta_1, \zeta_3) = (0, 0)$.

The energy budget is examined concerning the vortices near the shear layer found in Fig. 7. Figure 13 shows the profiles of $\overline{D_k}$ and $\overline{\varepsilon_k}$ on the ζ_2–ζ_3 plane at $\zeta_1 = 0$, where the isolines of $\overline{I_S}$ and $\overline{(\omega_R)}_{\zeta_1}$ mark the locations of the shear layer and the vortices, respectively. It is found from Figs. 7 and 13(a) that the regions with negative $\overline{D_k}$ have small $\overline{I_R}$. Thus, the source of the viscous transport of k toward the shear layer has a large mean velocity in the $\pm\zeta_3$ directions and is located outside the vortices with $\overline{(\omega_R)}_{\zeta_1} < 0$. As shown in Fig. 13(b), the dissipation actively occurs inside the shear layer, while the dissipation rate is small for the perimeter of the vortices, which is outside the shear layer.

The contribution of each velocity component to k is represented as $u_\alpha u_\alpha/2$, where the Greek letter in the subscript indicates that no summation is taken for the subscript. The transport equation for $u_\alpha u_\alpha/2$ contains the pressure–strain correlation term $\Pi_\alpha = p(\partial u_\alpha/\partial x_\alpha)$.[50] Because of $\Pi_x + \Pi_y + \Pi_z = 0$ due to incompressibility, Π_α is considered the redistribution term of the turbulent kinetic energy among different directions. This term evaluated in the shear coordinate is denoted by $\Pi_{\zeta_1} = p(\partial u_{\zeta_1}/\partial x_{\zeta_1})$, $\Pi_{\zeta_2} = p(\partial u_{\zeta_2}/\partial x_{\zeta_2})$, and $\Pi_{\zeta_3} = p(\partial u_{\zeta_3}/\partial x_{\zeta_3})$. In Fig. 14, the averages of Π_{ζ_i} are shown on the ζ_2–ζ_3 plane together with the isolines of $\overline{I_S}$ and $\overline{(\omega_R)}_{\zeta_1}$. Negative $\overline{\Pi_{\zeta_2}}$ appears near the shear layer, while $\overline{\Pi_{\zeta_1}}$ is mostly positive: the energy of the ζ_2 velocity component is converted to the ζ_1 component. This is consistent with Fig. 5(a), where the flow direction changes from $\pm\zeta_2$ to $\pm\zeta_1$ directions along the streamline estimated from the velocity vectors. Regions A in Figs. 14(b) and 14(c) have $\overline{\Pi_{\zeta_2}} < 0$ and $\overline{\Pi_{\zeta_3}} > 0$, and are located between the shear layer and the vortices. Thus, the velocity in the ζ_2 direction induced by the vortex is converted to the ζ_3 component, which is related to the flows in the $\pm\zeta_3$ directions besides the shear layer.

Figure 15(a) shows the mean profile of the advection term $\overline{T_k}$. The advection term is negative in region A, where $\overline{\Pi_{\zeta_2}} < 0$ and $\overline{\Pi_{\zeta_3}} > 0$ are found in Fig. 14. Below this region, positive $\overline{T_k}$ is found for $(\zeta_2/\eta, \zeta_3/\eta) \approx (\pm 3, \pm 5)$, and the energy is transferred in the parallel direction to the shear layer. This is better confirmed by the advection term by the mean velocity in the ζ_3 direction, which is written as $T_{m\zeta_3} = -\overline{u_3}(\partial \overline{k}/\partial \zeta_3)$ and is presented in Fig. 15(b). The profiles of $\overline{T_k}$ and $T_{m\zeta_3}$ are correlated with each other near the shear layer: two
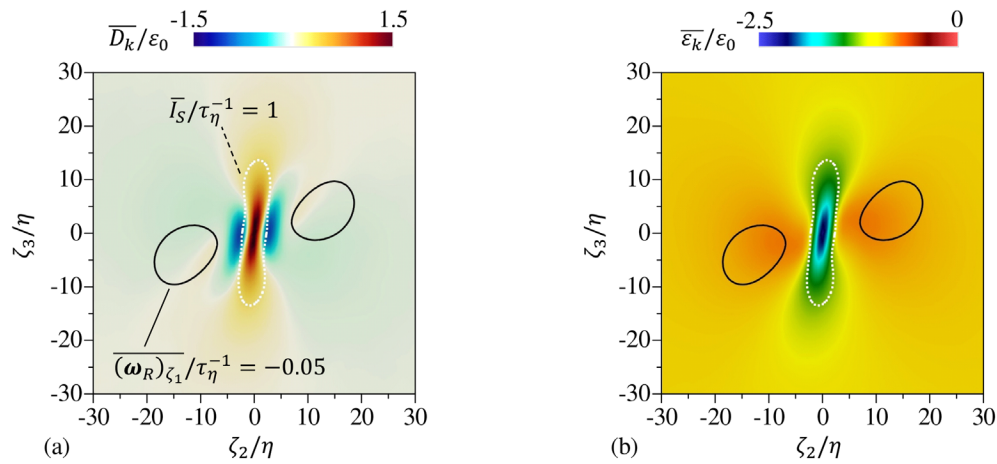
FIG. 13. Mean profiles of (a) viscous diffusion term D_k and (b) dissipation term ε_k on the ζ_2–ζ_3 plane at $\zeta_1 = 0$ in NS3. The dotted and solid lines represent the isolines of $\overline{I_S}$ and $\overline{(\omega_R)_{\zeta_1}}$.

pairs of positive and negative peaks of $\overline{T_k}$ near the shear layer are well captured by $T_{m\zeta_3}$. The energy of the shearing motion induced by the pressure–strain correlation in region A is transferred in the $\pm\zeta_3$ directions by the mean flow associated with the shear. This energy transport sustains the energetic fluid motions in the $\pm\zeta_3$ directions on both sides of the shear layer.

The above discussion of the energy transport by the vortices is valid even for the random velocity field because the relation between shear layers and nearby vortices is attributed to the kinematic relation. Figure 16 shows the advection by the mean flow in the ζ_3 direction, $T_{m\zeta_3}$, and the ζ_2 and ζ_3 components of the pressure–strain correlation ($\overline{\Pi_{\zeta_2}}$ and $\overline{\Pi_{\zeta_3}}$). The profiles near the shear layer qualitatively agree with the results for NS3 in Figs. 14(b), 14(c), and 15(b). The advection by the mean flow of shearing motion transfers the energy in the parallel direction of the shear layer. The kinetic energy of flow in the ζ_2 direction due to rotating motion is converted to that of the shear flow

in the $\pm\zeta_3$ direction by the pressure–strain correlation. Therefore, the mechanism that sustains shearing motion is embedded in the multi-scale random velocity field as the kinematic nature even though the random velocity does not obey the Navier–Stokes equations.

D. Development of shear layers in a random velocity field

The flow structures of strong shear in the random velocity are different from those in genuine turbulence in various aspects, such as the shape and the strain field around the shear layers. The development of shear layers is investigated for decaying turbulence initialized with the multi-scale random velocity field (D1-D3 in Table I). The statistics of shear layers are calculated as functions of time. As turbulence develops from the random velocity field, the characteristics of the shear layers become closer to those in isotropic turbulence.
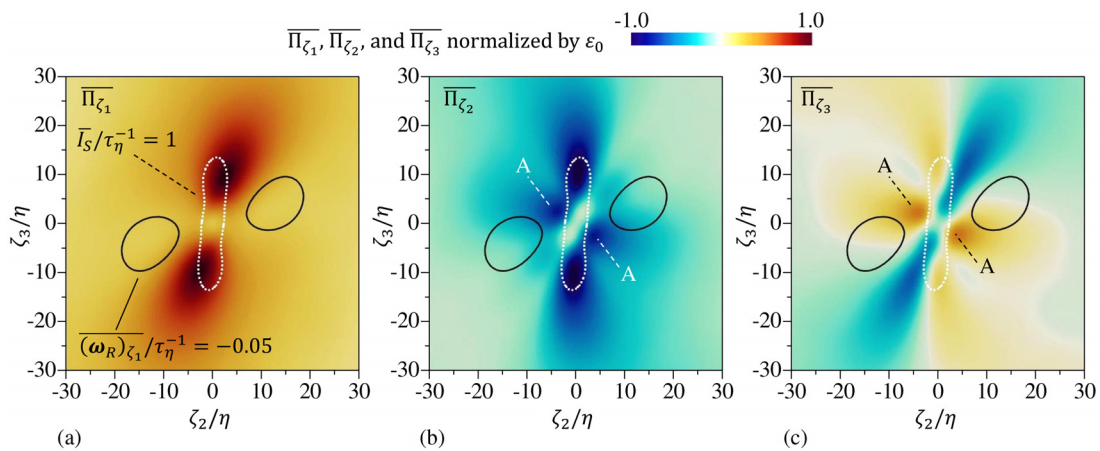

FIG. 14. Mean profiles of pressure–strain correlation terms (a) Π_{ζ_1}, (b) Π_{ζ_2}, and (c) Π_{ζ_3} on the ζ_2–ζ_3 plane at $\zeta_1 = 0$ in NS3. The dotted and solid lines are the same as in Fig. 13.
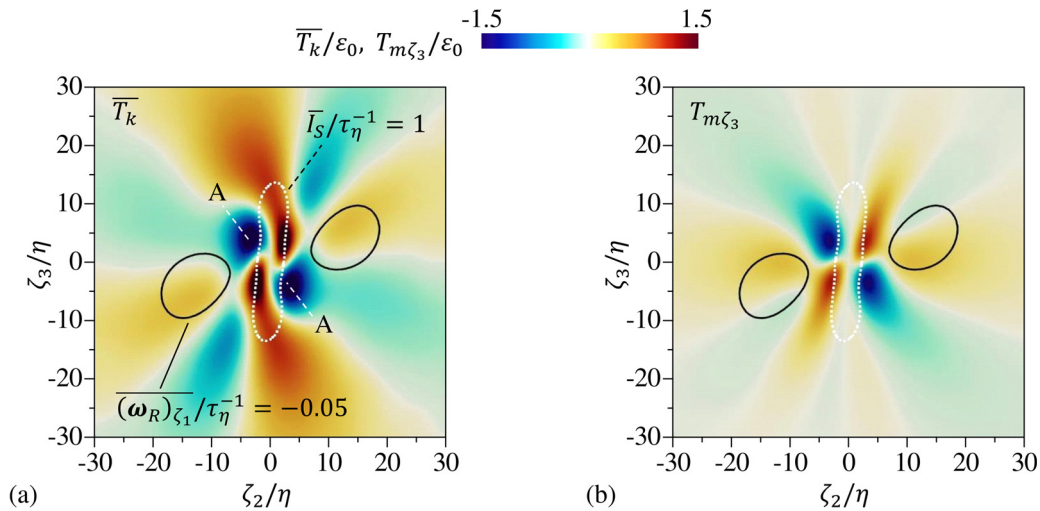
FIG. 15. (a) Averaged advection term of the turbulent kinetic energy equation (T_k); (b) advection term by the mean flow in the ζ_3 direction ($T_{m\zeta_3}$). The results are presented on the ζ_2–ζ_3 plane at $\zeta_1 = 0$ in NS3. The dotted and solid lines are the same as in Fig. 13.

The shape of the shear layer is examined with $\overline{I_S}(\zeta_1, \zeta_2, \zeta_3, t)$, for which a normalized mean shear intensity is defined as

$$\hat{I}_S(\zeta_1, \zeta_2, \zeta_3, t) = \frac{\overline{I_S}(\zeta_1, \zeta_2, \zeta_3, t) - \langle I_S\rangle(t)}{\overline{I_S}(0,0,0,t) - \langle I_S\rangle(t)}, \tag{18}$$

where $\langle I_S\rangle(t)$ is the volume average of I_S. The center of the shear layer at $(\zeta_1, \zeta_2, \zeta_3) = (0,0,0)$ has $\hat{I}_S = 1$, while $\hat{I}_S$ decreases to zero as ζ_i increases. At each time instance, we calculate the half width of $\hat{I}_S$, δ_{Si}, that is the distance between two locations of $\hat{I}_S = 0.5$ on each axis of ζ_i. Figure 17 shows the temporal evolution of δ_{Si}/η, where η is also evaluated at each instance as a function of time. Time is non-dimensionalized by the integral timescale or the Kolmogorov timescale at $t = 0$. At the initial state, the shear layer has $\delta_{S1} \approx \delta_{S3} \approx 5\eta$ and $\delta_{S2} \approx 3\eta$. As the flow evolves following the Navier–Stokes equations,

δ_{S2} decreases to 2.5η, while δ_{S1} and δ_{S3} increase. Thus, the shear layers are flattened with time. The anisotropic shape of $\delta_{S1} > \delta_{S3}$ is due to the stretching in the ζ_1 direction caused by the biaxial strain. A comparison between different Reynolds numbers indicates that the initial variation of δ_{Si}/η is better characterized by $\tau_{\eta 0}$ than T_{L0}. Thus, the timescale of the formation of the shear layers is characterized by the Kolmogorov timescale, suggesting that the shear layer formation is caused by small-scale velocity fluctuations. After $t/\tau_{\eta 0} \gtrsim 3$, the layer thickness, $\delta_{S2}/\eta \approx 2.5$, hardly varies with time. Similarly, δ_{S1}/η and δ_{S3}/η also weakly depend on t/τ_η at a late time.

The formation of the biaxial strain around the shear layer is examined with the mean velocity profile in the shear coordinate system. Figure 18 presents $\overline{u_{\zeta_2}}/u_\eta$ and $\overline{u_{\zeta_3}}/u_\eta$ on the ζ_2 axis ($\zeta_1 = \zeta_3 = 0$) and $\overline{u_{\zeta_1}}/u_\eta$ on the ζ_1 axis ($\zeta_2 = \zeta_3 = 0$). These velocity profiles are related to the shear and the biaxial strain. At $t = 0$, $\overline{u_{\zeta_1}}$ and
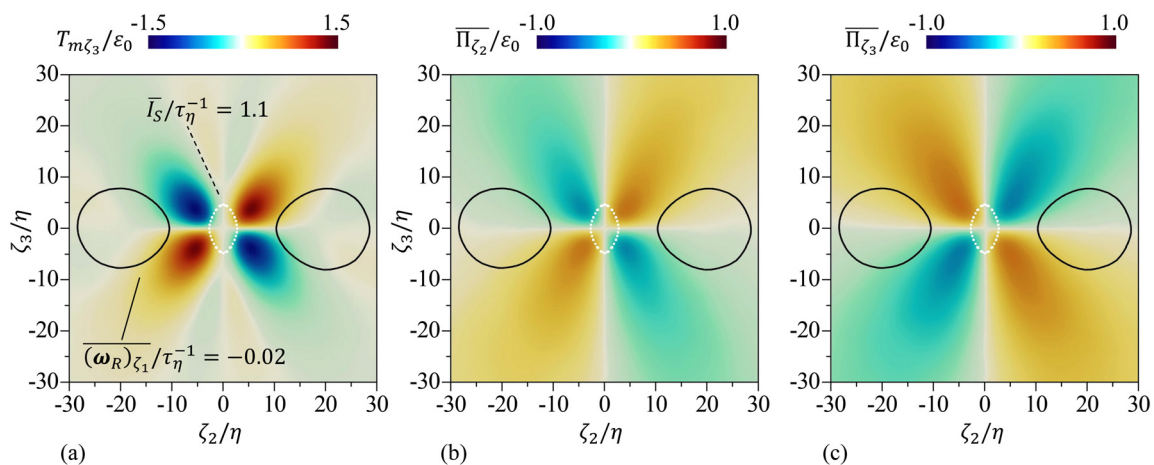

FIG. 16. Kinetic energy transport near shear regions in R3. (a) Advection term by the mean flow in the ζ_3 direction ($T_{m\zeta_3}$). Mean profiles of pressure–strain correlation terms: (b) $\overline{\Pi_{\zeta_2}}$ and (c) $\overline{\Pi_{\zeta_3}}$.
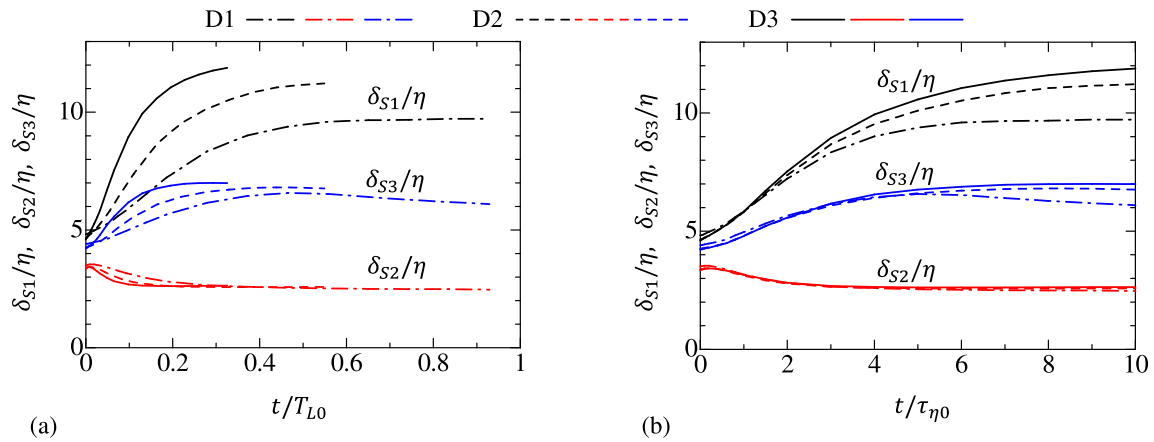
FIG. 17. Temporal evolutions of the length scales of the shear layer in three directions, δ_{S1}, δ_{S2}, and δ_{S3}, which are defined as the halfwidth of the normalized mean shear intensity, Eq. (18). Time is normalized by (a) integral timescale T_{L0} and (b) Kolmogorov timescale $\tau_{\eta 0}$.

$\overline{u_{\zeta_2}}$ are negligibly small because of the absence of the biaxial strain around the shear layer in the random velocity field. The mean velocity associated with shear, $\overline{u_{\zeta_3}}/u_\eta$, has large positive and negative peaks for $\zeta_2 > 0$ and $\zeta_2 < 0$, respectively. The profile of $\overline{u_{\zeta_3}}/u_\eta$ hardly varies with time although the peak locations slightly approach $\zeta_2 = 0$ since the shear layer becomes thin. Once the flow begins to evolve, $\overline{u_{\zeta_1}}$ and $\overline{u_{\zeta_2}}$ rapidly change with time. Here, $\partial\overline{u_{\zeta_1}}/\partial\zeta_1 > 0$ and $\partial\overline{u_{\zeta_2}}/\partial\zeta_2 < 0$ at the center of the shear layer indicate the biaxial strain with stretching in the ζ_1 direction and compression in the ζ_2 direction. The biaxial strain around the shear layer has fully developed at $t/\tau_{\eta 0} = 2$.

The mean velocity shown in Fig. 18 has positive and negative peaks. The difference between the peaks of $\overline{u_{\zeta_i}}$ is denoted by Δu_i. The thickness of the velocity jump is quantified as $\delta_{u1} = \Delta u_{\zeta_1}/|\partial\overline{u_{\zeta_1}}/\partial\zeta_1|$, $\delta_{u2} = \Delta u_{\zeta_2}/|\partial\overline{u_{\zeta_2}}/\partial\zeta_2|$, and $\delta_{u3} = \Delta u_{\zeta_3}/|\partial\overline{u_{\zeta_3}}/\partial\zeta_2|$ with the mean velocity gradient at the center of the shear layer. Figure 19 shows the temporal evolutions of $\Delta u_i/u_\eta$ and δ_{ui}/η. For all cases, $\Delta u_i/u_\eta$ reaches a steady state at $t/\tau_{\eta 0} \approx 3$. Large values of δ_{u1} and δ_{u2} at $t = 0$ are caused by the small mean velocity gradient and do not indicate that the length scale is infinitely large in these directions. The length δ_{ui} also approaches a steady state from $t = 0$. As Re increases from D1

to D3, δ_{u1}/η and δ_{u2}/η also increases. This Reynolds number dependence has also been observed in statistically steady isotropic turbulence.[13] However, $\delta_{u3}/\eta \approx 5$ hardly depends on the Reynolds number. The temporal evolutions of Δu_i and δ_{ui} suggest that the biaxial strain around the shear layer forms rapidly once the simulation is started from the random velocity field. The initial ratio between the integral timescale and the Kolmogorov timescale, $T_{L0}/\tau_{\eta 0}$, is 10.8, 18.2, and 30.8 in D1, D2, and D3, respectively. The time required for the formation of the biaxial strain is a few times the Kolmogorov timescale and is much shorter than the integral timescale. Therefore, the formation of the biaxial strain occurs even before large-scale velocity fluctuations fully develop from the random velocity field. This implies that the relation between the shear and the biaxial strain is established by small-scale velocity fluctuations rather than large-scale ones.

The behavior of the shear layers is expected to depend on the shear Reynolds number, which can be defined as $Re_S = \Delta u_3 \delta_{u3}/\nu$. Because $\Delta u_3 \approx 6u_\eta$ and $\delta_{u3} \approx 5\eta$ hardly vary with time, $Re_S \approx (6u_\eta)(5\eta)/\nu = 30$ is almost constant during the decay even though Re_λ decays with time. DNS of isotropic turbulence and turbulent planar jets has also confirmed that the shear Reynolds number hardly depends
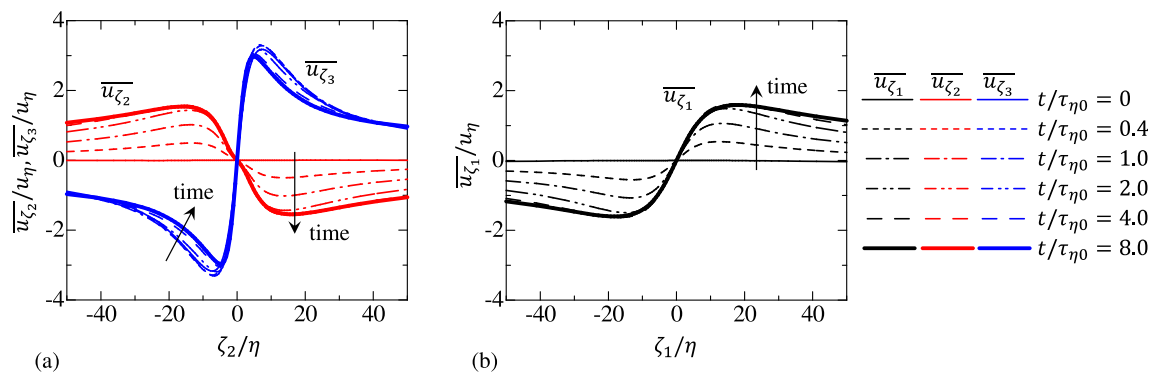

FIG. 18. Temporal evolutions of mean velocity profiles near the shear layer in D3. (a) $\overline{u_{\zeta_2}}$ and $\overline{u_{\zeta_3}}$ on the ζ_2 axis. (b) $\overline{u_{\zeta_1}}$ on the ζ_1 axis. The coordinates and velocity are normalized by time-dependent Kolmogorov length and velocity scales, η and u_η.
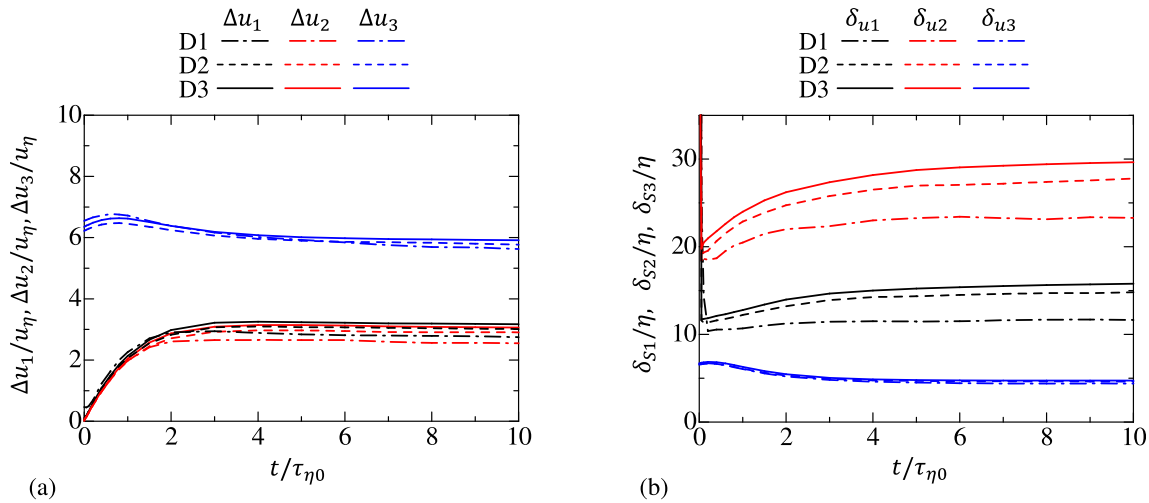
FIG. 19. Temporal evolutions of (a) mean velocity jumps Δu_i around the shear layers and (b) thickness δ_{ui} of the mean velocity jumps.

on Re_λ.[13,51] The development of shear layers is similar in all simulations with different Re_λ because of this weak Re_λ dependence of Re_S.

The formation of the compressive strain by $\partial \overline{u_{\zeta_2}}/\partial \zeta_2 < 0$ in the shear layer is examined with the mean velocity in the ζ_2 direction. Figure 20 visualizes $\overline{u_{\zeta_2}}$ with the isolines of $\overline{I_S}$ and $\overline{(\omega_R)}_{\zeta_1}$ at $t/\tau_{\eta 0} = 0$, 0.4, 1.0, and 2.0 for D3. At $t/\tau_{\eta 0} = 0$, $\overline{u_{\zeta_2}} > 0$ and $\overline{u_{\zeta_2}} < 0$ appear above and below the vortices on the sides of the shear layer. As also confirmed in Fig. 7(c), the mean velocity profile and the vortices locations are symmetric with respect to $\zeta_2 = 0$. Therefore, the compressive strain with $\partial \overline{u_{\zeta_2}}/\partial \zeta_2 < 0$ does not act at the center of the shear layer in the random velocity field at $t = 0$. As the flow evolves following the Navier–Stokes equations, this symmetry is immediately broken and the shear layer is tilted with respect to the nearby vortices. Then, the vortices begin to induce flow with $\overline{u_{\zeta_2}} > 0$ for $\zeta_2 < 0$ and $\overline{u_{\zeta_2}} < 0$ for $\zeta_2 > 0$, and the compressive strain of $\partial \overline{u_{\zeta_2}}/\partial \zeta_2 < 0$ is formed around the shear layer. The compressive strain caused by the nearby vortices is consistent with the sketch and flow visualization in Fig. 8. This change in the vorticity configuration also results in the formation of the extensive strain in the ζ_1 direction by the pressure–strain correlation shown in Fig. 14.

The formation of the shear layers from the random velocity field is visualized in Fig. 21. Intense shear regions appear as small spots without a layer shape at $t/\tau_{\eta 0} = 0$. The small spots rapidly grow into shear layers. One of the examples of the shear layer development is marked as A in the figure. The layer structures of shear are observed already at $t/\tau_{\eta 0} = 0.8$. Some intense shear regions marge during the formation of shear layers. The biaxial strain near the shear layer is rapidly established from the random velocity field by the small change in the configuration of vortices near shear layers. Therefore, the thin shear layers are also rapidly generated from the small spots of shear because they are compressed in the ζ_2 direction and stretched in the ζ_1 direction once the biaxial strain begins to act on the shear regions.

Figure 22 compares the initial profiles of u and I_S in D2F1 and D2F2 with those in D2. The initial conditions in D2F1 and D2F2 are generated with a filtered energy spectrum of NS2, for which the cutoff

wavenumbers are $k_F = 0.05/\eta = 3.9/L_0$ in D2F1 and $0.1/\eta = 7.8/L_0$ in D2F2. Thus, the cutoff length is smaller than the integral scale but larger than the Kolmogorov scale. Compared with the random velocity generated with the original spectrum in D2, velocity fluctuations in D2F1 and D2F2 are dominated by smaller scales and do not contain large-scale fluctuations. Since D2F2 uses a higher cutoff wavenumber than D2F1, the length scale of velocity fluctuations is smaller for D2F2 in Figs. 22(b) and 22(c). However, the cutoff wavenumbers in D2F1 and D2F2 are so small that the filters do not alter the small-scale characteristics. The initial velocity fields in D2, D2F1, and D2F2 have similar values of the Kolmogorov scale as shown as Δ/η in Table I, suggesting that the turbulent kinetic energy dissipation rate remains unchanged by the filter. Therefore, the initial profiles of the shear intensity are also qualitatively similar in Figs. 22(d)–22(f). Here, differences are caused by the random phases, which are different for the three cases. Figure 23 compares the temporal evolutions of the velocity jumps around the shear layers, Δu_1, Δu_2, and Δu_3. Here, Δu_i and t are normalized by the rms velocity fluctuations u_0 and the Kolmogorov timescale $\tau_{\eta 0}$ in NS2 from which the energy spectrum is taken to generate the random velocity fields. In turbulence, the kinetic energy at large scales is transferred to smaller scales, and small-scale motions are sustained even though the energy dissipation due to the viscous effects occurs at small scales. However, this energy transfer to the small scales lasts only for short time in D2F1 and D2F2 because the initial velocity field does not contain large-scale velocity fluctuations, which are eliminated by the filter. Therefore, the long-time behaviors of shear layers in D2F1 and D2F2 should differ from those in D2. However, the initial evolutions of Δu_1, Δu_2, and Δu_3 are similar for all simulations. The growth of Δu_1 and Δu_2, which is associated with the formation of the biaxial strain, occurs within a few times the Kolmogorov timescale even though large-scale fluctuations are absent in D2F1 and D2F2. This result suggests that the formation of shear layers with the biaxial strain is dominated by small-scale velocity fluctuations of turbulence.
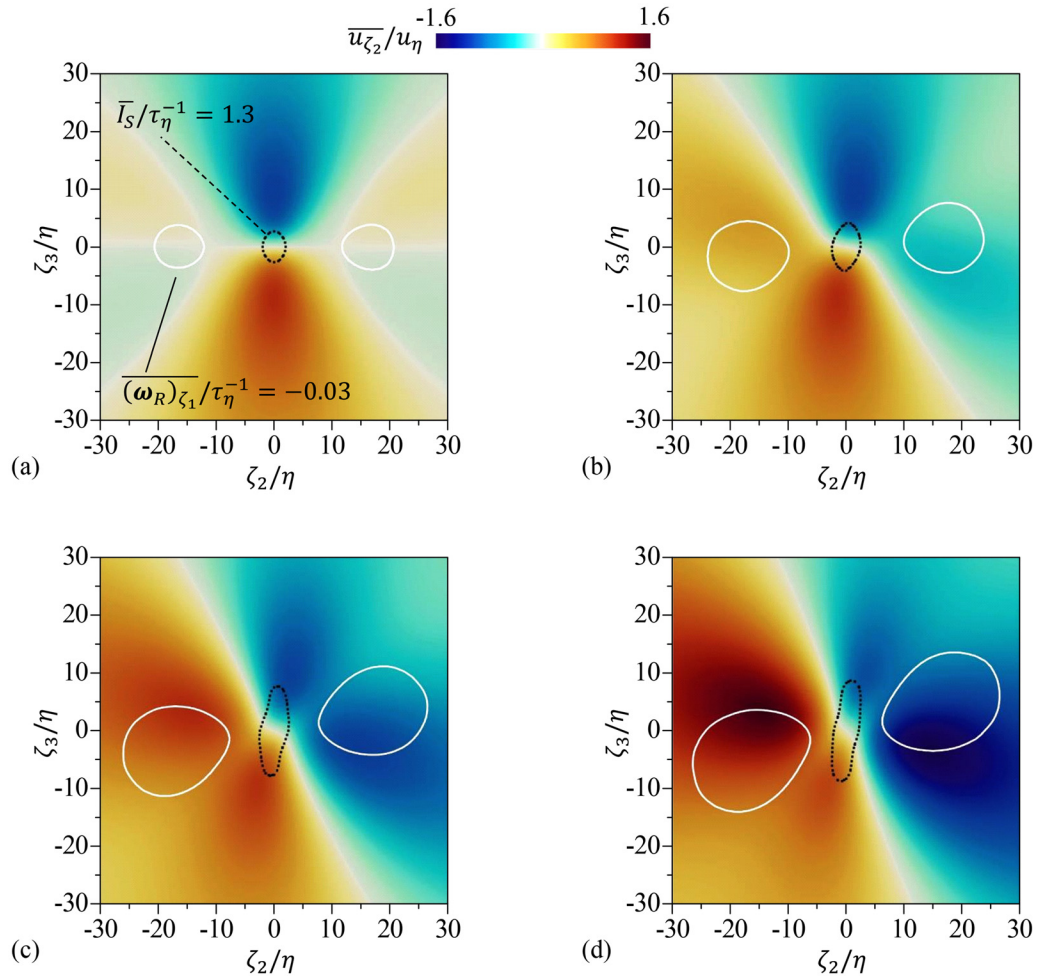
FIG. 20. Temporal evolution of the mean velocity in the ζ_2 direction, $\overline{u_{\zeta_2}}$, around the shear layers in D3: (a) $t/\tau_{\eta 0} = 0$; (b) $t/\tau_{\eta 0} = 0.4$; (c) $t/\tau_{\eta 0} = 1.0$; and (d) $t/\tau_{\eta 0} = 2.0$.
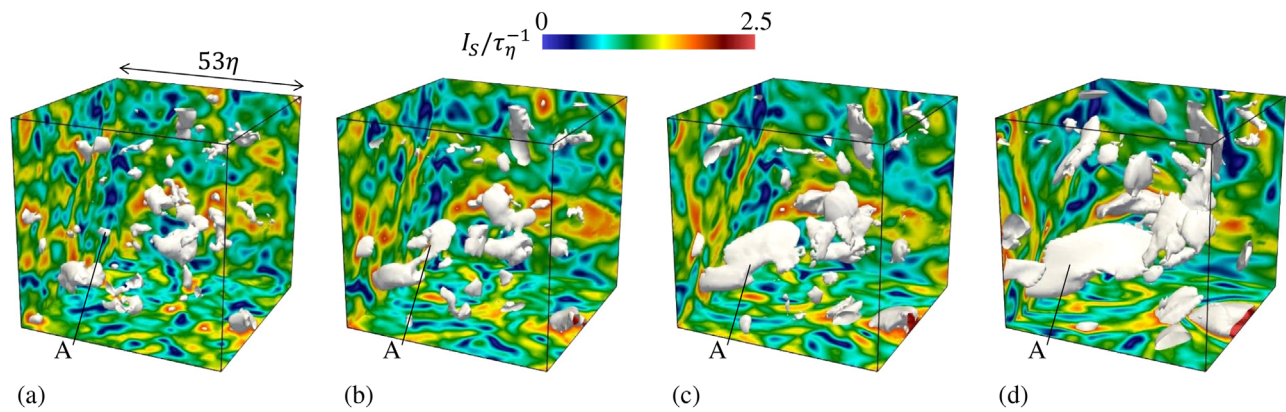

FIG. 21. The development of shear layers from a random velocity field. Isosurface of $I_S/(\tau_\eta^{-1}) = 2$ is visualized at (a) $t/\tau_{\eta 0} = 0$, (b) $t/\tau_{\eta 0} = 0.4$, (c) $t/\tau_{\eta 0} = 0.8$, and (d) $t/\tau_{\eta 0} = 1.5$.
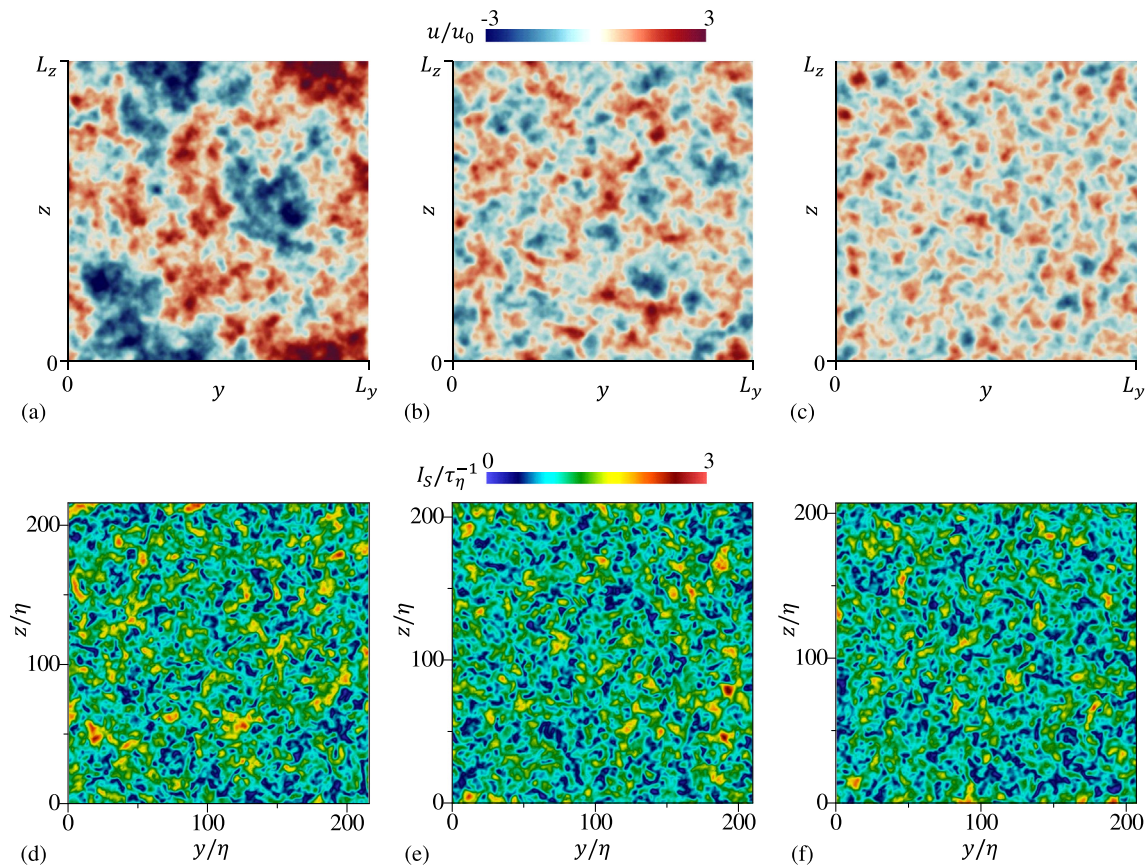
FIG. 22. Initial profiles of (a)–(c) velocity u and (d)–(f) shear intensity I_S in (a) and (d) D2, (b) and (e) D2F1, and (c) and (f) D2F2. A small part of the computational domain is shown for I_S, while u is visualized in the whole domain.

V. CONCLUSIONS

Small-scale shear layers in isotropic turbulence have been investigated with the triple decomposition of the velocity gradient tensor $\nabla \boldsymbol{u}$, which can identify the location and orientation of shear layers. Both clusters of shear layers and vortex tubes are intermittent in space, and their distributions are correlated with each other. The characteristics of shear layers are compared between isotropic turbulence and multiscale random velocity fields to reveal the role of kinematics in the formation of shear layers. Here, the random velocity possesses the energy spectrum of turbulence although they are not solutions of the Navier–Stokes equations.

The statistics of the shear layers have been evaluated in the reference frame defined with the shear orientation. Four circular regions with strong rotation were found near the shear layer in the mean profiles of shear and rotation intensities: two of them appear inside the shear layer and have the same vorticity direction as the shear vorticity; the others are located beside the shear layer and have the opposite vorticity direction. The same relation between shear and rotation has been found in the random velocity field, which is free from the dynamics of the Navier–Stokes equations. Vortex tubes are generated from the shear layers by shear instability, and the interplay between vortices and shear layers has been reported in previous studies.[15]

However, the configuration of rotating motions near shear layers is not attributed to this dynamical process but is related to the kinematic nature of velocity fluctuations.

The kinetic energy budget around the shear layer has suggested that the vortex beside the shear layer induces the energetic flow that contributes to the shear by pressure and advection. The shear layer is separated by a distance of about 12η from the vortex that induces the energetic flow in the proximity of the shear layer. Therefore, the energetic flow parallel to the shear layer exists between the vortex and shear layer, and the viscous and pressure diffusions transfer the kinetic energy toward the center of the shear layer, where the dissipation takes place. The mechanism that sustains shearing motion is embedded as the kinematic nature in the random velocity field because the configuration of shearing and rotating motions is similar between genuine turbulence and random velocity. Therefore, when decaying turbulence is simulated by using the random velocity field as an initial condition, initial intense shear regions do not disappear. In the random velocity field, the position of rotating motion that sustains the shear is right next to the shear layers. The vortex does not generate a compressive strain acting on the shear layer under this configuration of the structures. Once the initial random velocity field begins to evolve following the Navier–Stokes equations, the shear layer is immediately tilted to
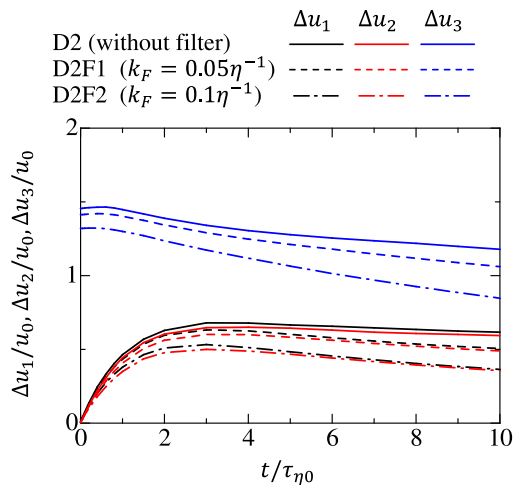
FIG. 23. Temporal evolutions of mean velocity jumps Δu_i in D2, D2F1, and D2F2. Time and velocity jumps are normalized with rms velocity fluctuations u_0 and Kolmogorov timescale $\tau_{\eta0}$ in NS2.

the nearby vortex. The tilted alignment is a key for the vortex to generate the compressive strain in the direction perpendicular to the shear layer and to form the biaxial strain around the shear layers. As the rotating motion that results in the formation of the biaxial strain appears even in the random velocity field, the thin shear layers subject to the biaxial strain are formed within a few Kolmogorov time scales after the flow begins to evolve from the initial random velocity field. The formation of the biaxial strain has also been examined in DNS initialized with high-pass filtered random velocity. The timescale of the formation of the biaxial strain is characterized by the Kolmogorov timescale even if the initial velocity field does not contain large-scale velocity fluctuations. Therefore, the formation of the biaxial strain around the shear layers is dominated by small-scale turbulent motions. These results indicate that the kinematic relation of rotation and shear in velocity fluctuations has a significant role in the formation of shear layers in turbulence.

ACKNOWLEDGMENTS

AUTHOR DECLARATIONS

Conflict of Interest

The authors have no conflicts to disclose.

Author Contributions

Tomoaki Watanabe: Conceptualization (lead); Data curation (lead); Formal analysis (lead); Funding acquisition (lead); Investigation (lead); Methodology (lead); Project administration (lead); Resources (lead); Software (lead); Validation (lead); Visualization (lead); Writing – original draft (lead). **Koji Nagata:** Conceptualization (supporting); Formal analysis (supporting); Funding acquisition (equal); Investigation (supporting); Methodology (supporting); Resources (supporting); Writing – review & editing (supporting).

DATA AVAILABILITY

The data that support the findings of this study are available from the corresponding author upon reasonable request.

REFERENCES

[1]P. A. Davidson, *Turbulence: An Introduction for Scientists and Engineers* (Oxford University Press, 2004).

[2]R. O. Fox, *Computational Models for Turbulent Reacting Flows* (Cambridge University Press, 2003).

[3]C. Meneveau, "Lagrangian dynamics and models of the velocity gradient tensor in turbulent flows," Annu. Rev. Fluid Mech. **43**, 219 (2011).

[4]G. K. Batchelor and A. A. Townsend, "The nature of turbulent motion at large wave-numbers," Proc. R. Soc. London A **199**, 238 (1949).

[5]C. Meneveau and K. R. Sreenivasan, "The multifractal nature of turbulent energy dissipation," J. Fluid Mech. **224**, 429 (1991).

[6]E. D. Siggia, "Numerical study of small-scale intermittency in three-dimensional turbulence," J. Fluid Mech. **107**, 375 (1981).

[7]J. Jiménez and A. A. Wray, "On the characteristics of vortex filaments in isotropic turbulence," J. Fluid Mech. **373**, 255 (1998).

[8]S.-J. Kang, M. Tanahashi, and T. Miyauchi, "Dynamics of fine scale eddy clusters in turbulent channel flows," J. Turbul. **8**, N52 (2007).

[9]S. Pirozzoli, M. Bernardini, and F. Grasso, "Characterization of coherent vortical structures in a supersonic turbulent boundary layer," J. Fluid Mech. **613**, 205 (2008).

[10]C. B. da Silva, R. J. N. Dos Reis, and J. C. F. Pereira, "The intense vorticity structures near the turbulent/non-turbulent interface in a jet," J. Fluid Mech. **685**, 165 (2011).

[11]R. Jahanbakhshi, N. S. Vaghefi, and C. K. Madnia, "Baroclinic vorticity generation near the turbulent/non-turbulent interface in a compressible shear layer," Phys. Fluids **27**, 105105 (2015).

[12]G. R. Ruetsch and M. R. Maxey, "Small-scale features of vorticity and passive scalar fields in homogeneous isotropic turbulence," Phys. Fluids **3**, 1587 (1991).

[13]T. Watanabe, K. Tanaka, and K. Nagata, "Characteristics of shearing motions in incompressible isotropic turbulence," Phys. Rev. Fluids **5**, 072601 (2020).

[14]D. Fiscaletti, O. R. H. Buxton, and A. Attili, "Internal layers in turbulent free-shear flows," Phys. Rev. Fluids **6**, 034612 (2021).

[15]K. Horiuti and T. Fujisawa, "The multi-mode stretched spiral vortex in homogeneous isotropic turbulence," J. Fluid Mech. **595**, 341 (2008).

[16]S. Pirozzoli, M. Bernardini, and F. Grasso, "On the dynamical relevance of coherent vortical structures in turbulent boundary layers," J. Fluid Mech. **648**, 325 (2010).

[17]V. Kolář, "Vortex identification: New requirements and limitations," Int. J. Heat Fluid Flow **28**, 638 (2007).

[18]C. Liu, Y. Gao, S. Tian, and X. Dong, "Rortex-A new vortex vector definition and vorticity tensor and vector decompositions," Phys. Fluids **30**, 035103 (2018).

[19]Y. Maciel, M. Robitaille, and S. Rahgozar, "A method for characterizing cross-sections of vortices in turbulent flows," Int. J. Heat Fluid Flow **37**, 177 (2012).

[20]W. Xu, Y. Gao, Y. Deng, J. Liu, and C. Liu, "An explicit expression for the calculation of the Rortex vector," Phys. Fluids **31**, 095102 (2019).

[21]Y. Gao, Y. Yu, J. Liu, and C. Liu, "Explicit expressions for Rortex tensor and velocity gradient tensor decomposition," Phys. Fluids **31**, 081704 (2019).

[22]Y.-Q. Wang, Y.-S. Gao, J.-M. Liu, and C. Liu, "Explicit formula for the Liutex vector and physical meaning of vorticity based on the Liutex-shear decomposition," J. Hydrodyn. **31**, 464 (2019).

[23]Y. Gao and C. Liu, "Rortex based velocity gradient tensor decomposition," Phys. Fluids **31**, 011704 (2019).

[24]X. Dong, Y. Gao, and C. Liu, "New normalized Rortex/vortex identification method," Phys. Fluids **31**, 011701 (2019).

[25]J. Liu and C. Liu, "Modified normalized Rortex/vortex identification method," Phys. Fluids **31**, 061704 (2019).

[26]J. Hoffman, "Energy stability analysis of turbulent incompressible flow based on the triple decomposition of the velocity gradient tensor," Phys. Fluids **33**, 081707 (2021).

[27]V. Kolář and J. Šístek, "Disappearing vortex problem in vortex identification: Non-existence for selected criteria," Phys. Fluids **34**, 071704 (2022).

[28]J. Eisma, J. Westerweel, G. Ooms, and G. E. Elsinga, "Interfaces and internal layers in a turbulent boundary layer," Phys. Fluids **27**, 055103 (2015).

[29]R. Nagata, T. Watanabe, K. Nagata, and C. B. da Silva, "Triple decomposition of velocity gradient tensor in homogeneous isotropic turbulence," Comput. Fluids **198**, 104389 (2020).

[30]D. K. Bisset, J. C. R. Hunt, and M. M. Rogers, "The turbulent/non-turbulent interface bounding a far wake," J. Fluid Mech. **451**, 383 (2002).

[31]C. B. da Silva and J. C. F. Pereira, "Invariants of the velocity-gradient, rate-of-strain, and rate-of-rotation tensors across the turbulent/nonturbulent interface in jets," Phys. Fluids **20**, 055101 (2008).

[32]O. R. H. Buxton, M. Breda, and K. Dhall, "Importance of small-scale anisotropy in the turbulent/nonturbulent interface region of turbulent free shear flows," Phys. Rev. Fluids **4**, 034603 (2019).

[33]K. F. Kohan and S. Gaskin, "The effect of the geometric features of the turbulent/non-turbulent interface on the entrainment of a passive scalar into a jet," Phys. Fluids **32**, 095114 (2020).

[34]R. Jahanbakhshi, "Mechanisms of entrainment in a turbulent boundary layer," Phys. Fluids **33**, 035105 (2021).

[35]R. Sahebjam, K. F. Kohan, and S. Gaskin, "The dynamics of an axisymmetric turbulent jet in ambient turbulence interpreted from the passive scalar field statistics," Phys. Fluids **34**, 015129 (2022).

[36]J. Šístek, V. Kolář, F. Cirak, and P. Moses, "Fluid-structure interaction and vortex identification," in *Proceedings of the 18th Australasian Fluid Mechanics Conference* (Australasian Fluid Mechanics Society Australia, 2012).

[37]V. Kolář and J. Šístek, "Recent progress in explicit shear-eliminating vortex identification," in *Proceedings of the 19th Australasian Fluid Mechanics Conference* (Australasian Fluid Mechanics Society Australia, 2014), pp. 8–11.

[38]L. Shtilman, M. Spector, and A. Tsinober, "On some kinematic versus dynamic properties of homogeneous turbulence," J. Fluid Mech. **247**, 65 (1993).

[39]A. Tsinober, *An Informal Conceptual Introduction to Turbulence* (Springer, 2009).

[40]T. Watanabe and K. Nagata, "Mixing model with multi-particle interactions for Lagrangian simulations of turbulent mixing," Phys. Fluids **28**, 085103 (2016).

[41]T. Watanabe, X. Zhang, and K. Nagata, "Turbulent/non-turbulent interfaces detected in DNS of incompressible turbulent boundary layers," Phys. Fluids **30**, 035102 (2018).

[42]T. Watanabe and K. Nagata, "Integral invariants and decay of temporally developing grid turbulence," Phys. Fluids **30**, 105111 (2018).

[43]Y. Morinishi, T. S. Lund, O. V. Vasilyev, and P. Moin, "Fully conservative higher order finite difference schemes for incompressible flow," J. Comput. Phys. **143**, 90 (1998).

[44]P. L. Carroll and G. Blanquart, "A proposed modification to Lundgren's physical space velocity forcing method for isotropic turbulence," Phys. Fluids **25**, 105114 (2013).

[45]J. C. Vassilicos, "Dissipation in turbulent flows," Annu. Rev. Fluid Mech. **47**, 95 (2015).

[46]C. Rosales and C. Meneveau, "Linear forcing in numerical simulations of isotropic turbulence: Physical space implementations and convergence properties," Phys. Fluids **17**, 095106 (2005).

[47]T. Watanabe, K. Tanaka, and K. Nagata, "Solenoidal linear forcing for compressible, statistically steady, homogeneous isotropic turbulence with reduced turbulent Mach number oscillation," Phys. Fluids **33**, 095108 (2021).

[48]K. Yamamoto, T. Ishida, T. Watanabe, and K. Nagata, "Experimental and numerical investigation of compressibility effects on velocity derivative flatness in turbulence," Phys. Fluids **34**, 055101 (2022).

[49]E. Johnsen, J. Larsson, A. V. Bhagatwala, W. H. Cabot, P. Moin, B. J. Olson, P. S. Rawat, S. K. Shankar, B. Sjögreen, H. C. Yee, X. Zhong, and S. K. Lele, "Assessment of high-resolution methods for numerical simulations of compressible turbulence with shock waves," J. Comput. Phys. **229**, 1213 (2010).

[50]S. B. Pope, *Turbulent Flows* (Cambridge University Press, 2000).

[51]M. Hayashi, T. Watanabe, and K. Nagata, "Characteristics of small-scale shear layers in a temporally evolving turbulent planar jet," J. Fluid Mech. **920**, A38 (2021).

[52]T. Watanabe, C. B. da Silva, Y. Sakai, K. Nagata, and T. Hayase, "Lagrangian properties of the entrainment across turbulent/non-turbulent interface layers," Phys. Fluids **28**, 031701 (2016).

[53]M. Hayashi, T. Watanabe, and K. Nagata, "The relation between shearing motions and the turbulent/non-turbulent interface in a turbulent planar jet," Phys. Fluids **33**, 055126 (2021).

[54]A. Attili, J. C. Cristancho, and F. Bisetti, "Statistics of the turbulent/non-turbulent interface in a spatially developing mixing layer," J. Turbul. **15**, 555 (2014).

[55]T. Watanabe, Y. Sakai, K. Nagata, Y. Ito, and T. Hayase, "Turbulent mixing of passive scalar near turbulent and non-turbulent interface in mixing layers," Phys. Fluids **27**, 085109 (2015).

[56]T. Watanabe, J. J. Riley, and K. Nagata, "Effects of stable stratification on turbulent/nonturbulent interfaces in turbulent mixing layers," Phys. Rev. Fluids **1**, 044301 (2016).

[57]T. Watanabe, J. J. Riley, S. M. de Bruyn Kops, P. J. Diamessis, and Q. Zhou, "Turbulent/non-turbulent interfaces in wakes in stably stratified fluids," J. Fluid Mech. **797**, R1 (2016).

[58]J. Philip, C. Meneveau, C. M. de Silva, and I. Marusic, "Multiscale analysis of fluxes at the turbulent/non-turbulent interface in high Reynolds number boundary layers," Phys. Fluids **26**, 015105 (2014).

[59]X. Zhang, T. Watanabe, and K. Nagata, "Turbulent/nonturbulent interfaces in high-resolution direct numerical simulation of temporally evolving compressible turbulent boundary layers," Phys. Rev. Fluids **3**, 094605 (2018).

[60]F. Moisy and J. Jiménez, "Geometry and clustering of intense structures in isotropic turbulence," J. Fluid Mech. **513**, 111 (2004).

[61]T. Ishihara, T. Gotoh, and Y. Kaneda, "Study of high–Reynolds number isotropic turbulence by direct numerical simulation," Annu. Rev. Fluid Mech. **41**, 165 (2009).

[62]O. R. H. Buxton and B. Ganapathisubramani, "Amplification of enstrophy in the far field of an axisymmetric turbulent jet," J. Fluid Mech. **651**, 483 (2010).

[63]M. Gul, G. E. Elsinga, and J. Westerweel, "Internal shear layers and edges of uniform momentum zones in a turbulent pipe flow," J. Fluid Mech. **901**, A10 (2020).

[64]G. E. Elsinga and I. Marusic, "Universal aspects of small-scale motions in turbulence," J. Fluid Mech. **662**, 514 (2010).

[65]G. E. Elsinga, T. Ishihara, M. V. Goudar, C. B. da Silva, and J. C. R. Hunt, "The scaling of straining motions in homogeneous isotropic turbulence," J. Fluid Mech. **829**, 31 (2017).

[66]C. P. Caulfield and W. R. Peltier, "The anatomy of the mixing transition in homogeneous and stratified free shear layers," J. Fluid Mech. **413**, 1 (2000).

[67]M. Abid and A. Verga, "Stability of a vortex sheet roll-up," Phys. Fluids **14**, 3829 (2002).

[68]G. M. Corcos and F. S. Sherman, "The mixing layer: Deterministic models of a turbulent flow. Part 1. Introduction and the two-dimensional flow," J. Fluid Mech. **139**, 29 (1984).

[69]S. J. Lin and G. M. Corcos, "The mixing layer: Deterministic models of a turbulent flow. Part 3. The effect of plane strain on the dynamics of streamwise vortices," J. Fluid Mech. **141**, 139 (1984).

[70]T. Watanabe, Y. Sakai, K. Nagata, Y. Ito, and T. Hayase, "Enstrophy and passive scalar transport near the turbulent/non-turbulent interface in a turbulent planar jet flow," Phys. Fluids **26**, 105103 (2014).

[71]T. S. Silva and C. B. da Silva, "The behaviour of the scalar gradient across the turbulent/non-turbulent interface in jets," Phys. Fluids **29**, 085106 (2017).